Inorganic Chemistry

pubs.acs.org/IC

Article

Effects of Structure and Bonding on ^{195}Pt Magnetic Shielding Tensors: Insights from Relativistic DFT and Localized Molecular Orbital Analysis

Sean T. Holmes, Adam B. Philips, Alberto Fernández-Alarcón, Jochen Autschbach,* and Robert W. Schurko*

Cite This: *Inorg. Chem.* 2026, 65, 4430−4445

Read Online

ACCESS | Metrics & More | Article Recommendations | Supporting Information

ABSTRACT: This study examines the use of density functional theory (DFT) calculations with a relativistic Hamiltonian for the prediction of ^{195}Pt NMR shielding tensors in coordination compounds, as well as the development and application of a method for obtaining quantitative relationships between ^{195}Pt chemical shift tensors and Pt−ligand bonding. We examine the importance of relativistic effects on ^{195}Pt magnetic shielding tensors, along with a representative GGA (PBE) and corresponding hybrid (PBE0) DFT functional approximation to determine what is necessary to achieve the best agreement with experiment without reliance upon fortuitous error cancellation. Two methodologies that address the issues of long-range effects on ^{195}Pt magnetic shielding tensors in solids are compared and contrasted: (i) calculations that treat the extended lattice of Pt-coordination compounds under periodic boundary conditions and (ii) all-electron calculations employing finite clusters as structural models. Natural bond orbital and natural localized molecular orbital analyses examining the contributions of individual orbitals to the ^{195}Pt magnetic shielding tensors are used to understand their relationship to the electronic structure and Pt−ligand bonding. Finally, the potential of these theoretical methods for investigating a wide range of materials containing platinum group elements is discussed.

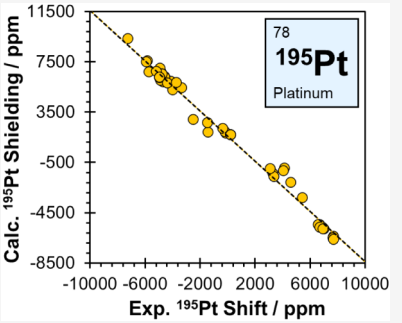

1. INTRODUCTION

Owing to their distinctive physicochemical properties, the platinum group elements (PGEs; Ru, Rh, Pd, Os, Ir, and Pt) play essential roles in critical technologies, including catalysis, electronic devices, and medical applications.[1−5] Some of the unique properties of PGE coordination compounds result from their distinctive dative bonding, i.e., covalent bonding by ligand-to-metal donation and metal-to-ligand back-donation of electrons.[6,7] Unfortunately, PGEs are scarce and costly; therefore, there is a pressing need to identify abundant and cheap alternatives to replace PGEs in technologically relevant materials. A possible pathway to finding replacement metals is through the discovery of unique ligands that compensate for bonding contributions particular to specific PGE−ligand bonds.[8,9] With this goal in mind, it is necessary to gain a deeper understanding of the nature of PGE−ligand bonding, as this may inform rational strategies for replacing PGEs and designing materials with tunable properties. The present work focuses on the namesake of the PGEs, i.e., platinum, and its coordination compounds.

The combination of solid-state NMR (SSNMR) spectroscopy and quantum chemical computations using density functional theory (DFT) with a relativistic Hamiltonian provides one important avenue for investigating PGE−ligand bonding, since NMR parameters are very sensitive to the composition of bonding, antibonding, and nonbonding molecular orbitals.[10−17] Among the platinum group elements, ^{195}Pt is the most extensively characterized by SSNMR due to its moderate receptivity, with numerous reports detailing its application to a wide range of materials.[18−34] However, the large chemical shift anisotropies observed for many Pt complexes present significant challenges for spectral acquisition and interpretation.[35] Wideline and ultrawideline (i.e., patterns with breadths ≥250 kHz) ^{195}Pt SSNMR powder patterns can be acquired using a variety of methods, including those utilizing direct excitation,[36−40] polarization transfer from more abundant spins,[41−43] and indirect detection through abundant spins.[44−48] In contrast, for the other PGEs, there are very few (^{103}Rh, $^{99/101}$Ru, and ^{105}Pd)[49−55] or no ($^{187/189}$Os and $^{191/193}$Ir) reports of their SSNMR spectra, largely due to their comparatively low receptivity to the NMR experiment. However, recent publications from our laboratories have reported optimized experimental conditions for acquiring ^{103}Rh and ^{99}Ru SSNMR spectra to elucidate the nature of PGE−ligand bonding.[53−55]

Received: November 3, 2025
Revised: January 20, 2026
Accepted: January 23, 2026
Published: February 17, 2026

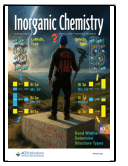

Quantum chemical computations increasingly permit accurate prediction of the electronic and magnetic properties of materials. Relativistic DFT methods can predict the magnetic shielding tensors for fifth- and sixth-period elements and relate them to experimental chemical shift tensors with a high degree of accuracy, affording opportunities to determine which individual orbitals most strongly influence ^{195}Pt magnetic shielding tensors and by extension, their relationship to molecular-level structure and Pt−ligand bonding.[25,53,56−63] The factors underlying these relationships have been explored in terms of contributions from different localized molecular orbitals,[12] revealing four key influences: (i) differences between (pseudo-) square planar and (pseudo-)octahedral coordination geometries (i.e., Pt^{II} and Pt^{IV} species, respectively); (ii) the extent of delocalization of nonbonding Pt 5d lone pair orbitals; (iii) the delocalization of Pt−ligand bonds; and (iv) the occupancy of antibonding Pt−ligand σ^* orbitals.

Computations of ^{195}Pt magnetic shielding tensors have garnered significant interest because of the large ^{195}Pt chemical shift range (>15 000 ppm in diamagnetic compounds) and the importance of relativistic effects.[21,25−29,64−78] Much prior work has focused on the comparison of calculated Pt NMR parameters with experimental data obtained from solution NMR. However, these calculations are complicated by a range of factors that influence their outcomes. ^{195}Pt chemical shifts are very challenging to compute due to their high sensitivity to relativistic effects, basis set quality, the chosen (or required) density functional, molecular geometry (especially the Pt−ligand distances), and potential solvent effects (including solvent−solute dynamics). These interdependent factors complicate the assessment of computational accuracy, as it is often unclear which of these influences dominate discrepancies with experimental data.

Among the available approaches to treat relativistic effects, the quasi-relativistic zeroth-order regular approximation (ZORA) Hamiltonian, which treats scalar relativistic (SR) as well as spin−orbit (SO) relativistic effects, has emerged as a practical and widely adopted approach for the calculation of NMR interaction tensors.[76] Several studies have demonstrated that ZORA yields accurate NMR chemical shifts and *J*-couplings for ^{195}Pt and other heavy elements in benchmark comparisons to fully relativistic methods.[79−86] As for DFT approximations, hybrid functionals are expected to perform significantly better than nonhybrid functionals for the calculation of NMR parameters of transition metal complexes.[87]

Accurately calculating ^{195}Pt chemical shifts remains a challenge due to the complex interplay of environmental effects in both solution and solid phases. In solution-phase NMR calculations, solvation and dynamical averaging can introduce substantial sources of error that obscure the true performance of an otherwise well-constructed computational approach.[74,75,77,78] In the present work, these complications are avoided by focusing on the ^{195}Pt chemical shift data obtained from SSNMR spectra, where solvent effects are absent. However, this brings its own challenges, requiring a thorough assessment of the treatment of solid-state crystal packing and long-range electrostatic effects.[21,25,28,29]

Recently, implementations for NMR shielding tensors using DFT with the ZORA Hamiltonian and periodic boundary conditions (PBCs, such as in the GIPAW approach), including SO effects, have been reported.[88,89] These methods are certainly suitable for assessing the long-range effects from periodic environments and the principal magnitudes of SO effects. However, the cited implementations do not yet support hybrid functionals such as PBE0, which are known to improve NMR shielding calculations substantially.[90] Furthermore, we have not been able to verify whether the crucial response of the XC potential to one of the perturbations (nuclear spin magnetic moment or the external field),[82] which has to be solved self-consistently in the presence of the SO interaction irrespective of whether the XC approximation includes exact exchange or not, is implemented fully in the available PBC codes. It is also worth noting that a "finite field" style implementation, using the nuclear magnetic moment as the perturbation according to the "converse approach" used for most NMR codes with PBCs, is unlikely to be variationally stable for heavy nuclei such as Pt when sufficiently flexible basis sets are used.[91] Finally, the available PBC NMR codes do not feature the kind of analysis tools in terms of localized MOs as used in the present work. Given these caveats, we found it more suitable to approximate the crystal environments in molecular calculations via finite cluster models while treating the magnetic field response fully analytically and having the possibility of employing hybrid functionals and localized MO analyses, instead of employing one of the available PBC codes along with the approximations accompanying these implementations.

This study is motivated by the desire to establish chemically intuitive methods for correlating ^{195}Pt chemical shift tensors to bonding and structure by using relativistic DFT calculations in comparison with experimental SSNMR data. The growing literature on Pt NMR calculations suggests that relativistic effects, hybrid functionals, and solid-state effects are all essential for accurate modeling. Thus, a computational strategy that balances accuracy, interpretability, and structural fidelity is needed. The present work adopts such a "best of both worlds" approach, which leverages molecular-level calculations with interpretive power, while using cluster models that approximate the local lattice environment. Critical considerations for conducting such calculations on Pt^{II} and Pt^{IV} coordination compounds that lead to the best agreement with experiment are explored, including: (i) the importance of treating SO effects, which substantially complicate the development of methods and render the calculations more expensive; (ii) the choice of exchange-correlation functional; and (iii) the computational protocol for accounting for intermolecular effects in molecular solids. The relationships between ^{195}Pt chemical shift tensors, structure, and bonding are investigated using both natural localized molecular orbital (NLMO) and natural bond orbital (NBO) analyses, which provide chemically intuitive insight into the individual orbital contributions to the NMR interaction tensors.[11−13,92] Finally, we discuss the general applicability of these computational methods for the study of the NMR interaction tensors of other PGEs and their ligands and their use for determining structure−property−function relationships.

2. COMPUTATIONAL METHODS

2.1. Geometry Optimizations

Structural refinements were performed using plane-wave DFT as implemented in the CASTEP module of Materials Studio 2020.[93] These calculations were performed on model structures obtained from neutron or X-ray diffraction studies (Table S1, Supporting Information), for which the positions of all atoms were relaxed using the quasi-Newton LBFGS energy-minimization scheme,[94] whereas lattice parameters remained fixed at their experimental values. Calculations employed the PBE functional[95] with a plane-wave cutoff energy of 800 eV and core−valence interactions modeled with ultrasoft

https://doi.org/10.1021/acs.inorgchem.5c05169
Inorg. Chem. 2026, 65, 4430−4445

pseudopotentials[96] generated on the fly. Relativistic effects were incorporated using the ZORA pseudopotential formalism.[97] Integrals over the Brillouin zone were sampled using a Monkhorst–Pack grid with a k-point spacing of 0.05 $Å^{-1}$.[98] Semiempirical dispersion was included through the many-body dispersion force field approximation of Tkatchenko et al.[99] Thresholds for assessing structural convergence were a maximum change in energy of 5×10^{-6} eV $atom^{-1}$, a maximum displacement of 5×10^{-4} Å $atom^{-1}$, and a maximum Cartesian force of 10^{-2} eV $Å^{-1}$.

2.2. Overview of Magnetic Shielding Calculations

All ^{195}Pt magnetic shielding tensors were calculated from the energy-minimized structural models obtained from the CASTEP geometry optimizations. Magnetic shielding tensors were calculated using either CASTEP[93] or the Amsterdam Density Functional (ADF) program included in the AMS suite (AMS 2021),[100,101] with different computational protocols depending on the software package and the nature of the crystal structure. Plane-wave DFT calculations in CASTEP employed the PBE functional, the gauge-invariant projector-augmented wave (GIPAW) approach of Pickard and Mauri,[102,103] and otherwise identical parameters and approximations as those used in the geometry optimizations. Convergence of ^{195}Pt magnetic shielding tensors with respect to the plane-wave cutoff energy and k-point spacing is demonstrated by the data in Table S2. Calculations of magnetic shielding tensors with free boundary conditions (finite systems) employed the gauge-including atomic orbital (GIAO) method,[104,105] as implemented in AMS.[69,106−109] These calculations used either the PBE[95] or hybrid PBE0[90,110] functional, and the ZORA Hamiltonian in its scalar relativistic (SR) approximation or in its full form including both scalar relativistic effects and the spin–orbit (SO) interaction.[76,111,112−114] In the SO calculations, the NMR step included the response of the DFT exchange-correlation potential.[82,115] Calculations of magnetic shielding in AMS used both isolated molecules and clusters of molecules as structural models, as outlined below.

2.3. Methods for Calculating Shielding for Molecular Solids

For calculations of ^{195}Pt magnetic shielding tensors in molecular solids, clusters of molecules were constructed to represent the local environment of the complexes in the crystals, as described previously.[61,116−118] Each cluster consists of a central complex ion for which the ^{195}Pt magnetic shielding tensors are computed, as well as a coordination shell consisting of between eight and 14 complete peripheral molecules, depending on the material (Scheme 1). A layered

Scheme 1. Molecular Clusters for Cisplatin and Transplatin Representing the Complete Coordination Shell Around a Central Molecule[a]

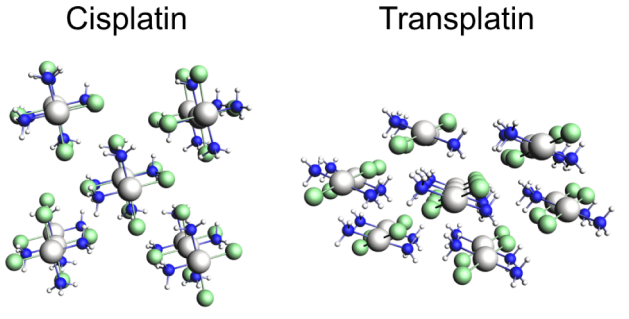

[a]Atomic coloring scheme: silver = Pt; green = Cl; blue = N; white = H.

scheme was used for the basis set and numerical quality of the integration grid[119,120] as follows: (i) for nonhydrogen atoms in the molecule of interest, a triple-ζ Slater-type orbital basis set with two polarization functions optimized for ZORA calculations (TZ2P) was employed, along with a numerical grid set to "good"; (ii) for all other atoms, a "basic" grid was used; (iii) Pt atoms in the peripheral molecules of the clusters were treated with a double-ζ polarized basis (DZP), while a minimal basis (SZ) was used for the other atoms in the cluster as well as for hydrogens in the ligands of the central molecule. In some cases, it was necessary to change the integration grid for the DZP and SZ regions to "normal" to achieve SCF convergence.

2.4. Methods for Calculating Shielding in Network Solids

Calculations of ^{195}Pt magnetic shielding tensors for network solids employed the valence modification of terminal atoms using bond valence theory (VMTA/BV) approximation, which was first introduced for the study of lead-containing materials[59] and has been employed successfully for the calculation of the magnetic shielding tensors of a variety of nuclides.[56,57,60,61,121,122] In this approximation, clusters of atoms are expanded around a central atom, leading to large net charges due to missing counterions coordinating the terminal atoms (Scheme 2). To compensate for this, the standard nuclear charges on the

Scheme 2. Third Coordination Shell Clusters for $K_2[PtCl_4]$ and $K_2[PtCl_6]$[a]

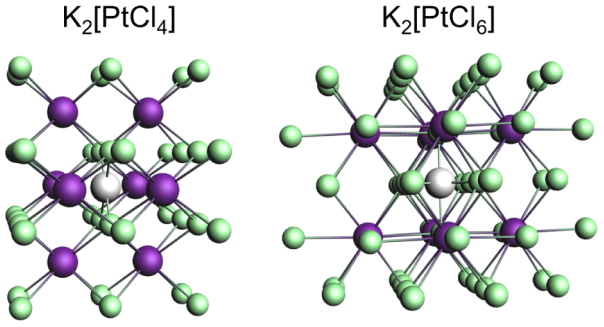

[a]Atomic coloring scheme: silver = Pt; green = Cl; purple = K.

terminal atoms of the clusters (Z_{nuc}) are modified (Z_{mod}) by the additional term (ΔS) that accounts for the missing bonds resulting from the termination of the cluster:

$$Z_{mod} = Z_{nuc} + \Delta S \quad (1)$$

The values of Z_{mod} are summarized in Table S3. Unless stated otherwise, clusters of network solids were constructed to consist of up to three coordination shells around the central Pt site, as clusters of this size present a satisfactory trade-off between accuracy and computational cost.[59,122] These calculations used a basis set-partitioning scheme in which the central Pt atom and all directly bonded atoms were assigned the TZ2P basis set, with the numerical grid set to "good", and all atoms up to the third coordination shell were assigned the SZ basis set (or DZP and DZ for heavy Pt and Cs atoms, respectively), with the numerical quality set to "basic".

2.5. NBO and NLMO Analysis

Localized molecular orbital (MO) analyses of the platinum shielding tensors were performed on top of the finite-cluster calculations with the ADF program. In each case, an initial calculation at the ZORA/SR level was performed to obtain a set of SR canonical MOs. Orbital localization was then performed via the NBO 6.0 program interfaced with ADF.[14,123] The NBO step was followed by a DFT calculation at the SO (including SR effects) level. The shielding tensor at the Pt nucleus was then calculated using the NMR module of ADF and analyzed in terms of contributions from the SR NBOs, as well as the corresponding NLMOs, as detailed elsewhere.[11−13] Note that the full set of NBOs and NLMOs is used in the calculations, such that the change of basis does not constitute an approximation.

2.6. Statistical Analysis

The relationship between calculated principal components of the magnetic shielding tensors ($\sigma_{ii}^{v,calc}$) and experimental principal components of chemical shift tensors ($\delta_{ii}^{v,exp}$) is described by the following expression:

https://doi.org/10.1021/acs.inorgchem.5c05169
Inorg. Chem. 2026, 65, 4430−4445

Table 1. Experimental and Calculated ^{195}Pt Chemical Shift Tensors for Cisplatin and Transplatin as Modeled Using Molecular Clusters of Increasing Size[abc]

	δ_{11} (ppm)	δ_{22} (ppm)	δ_{33} (ppm)	δ_{iso} (ppm)	Ω (ppm)	κ	d_v (ppm)
Cisplatin							
Experimental	3816	−4574	−4745	−1834	8561	−0.96	-
Isolated molecule	1640	−4142	−5125	−2542	6765	−0.71	988
Small cluster (3 molecules)	2150	−4004	−5006	−2287	7156	−0.72	738
Medium cluster (9 molecules)	2425	−4052	−4986	−2205	7411	−0.75	620
Full cluster (15 molecules)	2430	−4156	−5014	−2246	7444	−0.77	625
Transplatin							
Experimental	3279	−4001	−5821	−2181	9100	−0.60	-
Isolated molecule	247	−4204	−5187	−3048	5434	−0.64	1317
Small cluster (3 molecules)	2413	−4475	−5056	−2373	7469	−0.84	480
Medium cluster (7 molecules)	2916	−3931	−5740	−2252	8656	−0.58	149
Full cluster (15 molecules)	2840	−3857	−5824	−2280	8664		185

[a]The chemical shift tensors are defined with the principal components ordered from highest to lowest frequency as $\delta_{11} \geq \delta_{22} \geq \delta_{33}$. The Herzfeld−Berger convention is also used herein, where the isotropic chemical shift, span, and skew are given by $\delta_{iso} = (\delta_{11} + \delta_{22} + \delta_{33})/3$, $\Omega = \delta_{11} - \delta_{33}$, and $\kappa = 3(\delta_{22} - \delta_{iso})/\Omega$, respectively. [b]Calculations were performed using the hybrid PBE0 functional, the ZORA spin−orbit relativistic treatment, and a cluster of molecules representing the local lattice environment. See the main text for further details. Calculated values were converted to the chemical shift scale following the discussion in Section 2.6. [c]Chemical shift distance (d_v) between the experimental and calculated chemical shift tensors is given by eq 4.

$$\sigma_{ii}^{v,\mathrm{calc}} = A\delta_{ii}^{v,\mathrm{exp}} + B \tag{2}$$

where the index v denotes the Pt site ($v = 1, 2, ..., N$), the index i denotes the principal component of the shielding tensor (i = 1, 2, 3), A represents the slope of the correlation line, and B represents the interpolated shielding of the *reference state* [1.0 M Na_2PtCl_6(aq) at $\delta_{iso}(^{195}\mathrm{Pt}) = 0.0$ ppm]. Calculated chemical shifts ($\delta_{ii}^{v,\mathrm{calc}}$) are derived from the following expression:

$$\delta_{ii}^{v,\mathrm{calc}} = (B - \sigma_{ii}^{v,\mathrm{calc}})/A \tag{3}$$

The *chemical shift distance* for atom v, d_v, provides a comparison between a calculated and an experimental chemical shift tensor with a single scalar value in ppm. Given two sets of principal components of chemical shift tensors, d_v is defined by the following expression:[124]

$$d_v = \left(\frac{1}{15}[3(\delta_{11}^{v,\mathrm{calc}} - \delta_{11}^{v,\mathrm{exp}})^2 + 3(\delta_{22}^{v,\mathrm{calc}} - \delta_{22}^{v,\mathrm{exp}})^2 + 3(\delta_{33}^{v,\mathrm{calc}} - \delta_{33}^{v,\mathrm{exp}})^2 + 2(\delta_{11}^{v,\mathrm{calc}} - \delta_{11}^{v,\mathrm{exp}})(\delta_{22}^{v,\mathrm{calc}} - \delta_{22}^{v,\mathrm{exp}}) + 2(\delta_{11}^{v,\mathrm{calc}} - \delta_{11}^{v,\mathrm{exp}})(\delta_{33}^{v,\mathrm{calc}} - \delta_{33}^{v,\mathrm{exp}}) + 2(\delta_{22}^{v,\mathrm{calc}} - \delta_{22}^{v,\mathrm{exp}})(\delta_{33}^{v,\mathrm{calc}} - \delta_{33}^{\mathrm{exp}})]\right)^{1/2} \tag{4}$$

A root-mean-square chemical shift distance for the N chemical shift tensors (Δ_{RMS}) is determined by the following expression:

$$\Delta_{RMS} = \left(\frac{1}{N}\sum_{v=1}^{N} d_v^2\right)^{1/2} \tag{5}$$

The values for the shielding of the reference system, B, and the slope, A, are optimized numerically via a generalized reduced gradient algorithm for each type of calculation to minimize the value of Δ_{RMS}.

3. RESULTS AND DISCUSSION

3.1. Overview

^{195}Pt magnetic shielding tensors were calculated for crystalline, diamagnetic solids containing Pt atoms in the Pt^{II} and Pt^{IV} oxidation states. We first assess the quality of the results through a comparison with experimental ^{195}Pt chemical shift tensors. Several technical aspects related to the construction of solid-state clusters to model local crystal environments and their impact on the calculations of ^{195}Pt magnetic shielding tensors for representative cases are outlined in Section 3.2. This analysis is expanded in Section 3.3 to the ^{195}Pt magnetic shielding tensors for 16 systems, along with an exploration of the importance of relativistic approximations and the choice of density functional for achieving agreement with experimental values. Finally, NBO/NLMO analyses of contributions of individual orbitals to the ^{195}Pt magnetic shielding tensors are discussed in Section 3.4 to understand their relationship to structure and bonding, focusing on a representative subset of materials. Calculations described in Sections 3.2 and 3.4 are performed at the PBE0/SO level, whereas those in Section 3.3 are performed at various levels of theory.

3.2. ^{195}Pt Magnetic Shielding Tensors for Select Systems

In this section, we discuss technical aspects related to the construction of solid-state cluster models to represent local crystal environments and their impact on calculations of ^{195}Pt magnetic shielding tensors, with the goal of finding the best trade-off between accuracy and computational cost.

3.2.1. Molecular Solids. For square-planar Pt^{II} complexes with low-molecular-weight ligands residing in the L_4Pt plane, it is anticipated that intermolecular interactions will have a significant influence on the ^{195}Pt magnetic shielding tensors due to interactions between the Pt atom and nearby molecules.[25] The comparison of calculations on different structural models of cisplatin [*cis*-$PtCl_2(NH_3)_2$] and transplatin [*trans*-$PtCl_2(NH_3)_2$] provides a means of establishing the importance of intermolecular effects because of differences in the packing arrangements that these molecules adopt (Scheme 1). For instance, cisplatin molecules pack in a columnar fashion, with Pt−Pt intermolecular interactions between Pt^{II} centers, whereas transplatin lacks Pt−Pt interactions, instead featuring intermolecular contacts between Pt and the amine and chlorine ligands.[125]

We have explored four methods of probing intermolecular effects on ^{195}Pt magnetic shielding tensors via calculations on: (i) *isolated molecules* for which all intermolecular interactions are ignored; (ii) *small molecular clusters* that account for only the shortest Pt−Pt and/or Pt−L (L = Cl, NH_3) contacts; (iii) *medium molecular clusters* that account for all Pt−L contacts up to *ca.* 5 Å; and (iv) *large molecular clusters* that account for all

https://doi.org/10.1021/acs.inorgchem.5c05169
Inorg. Chem. 2026, 65, 4430−4445

Table 2. Experimental and Calculated ^{195}Pt Chemical Shift Tensors for $K_2[PtCl_4]$ and PtS as Modeled Using Different Sizes of Clusters and Modified (VTMA/BV) or Standard Nuclear Charges[a]

	δ_{11} (ppm)	δ_{22} (ppm)	δ_{33} (ppm)	δ_{iso}(ppm)	Ω (ppm)	κ	d_v (ppm)
$K_2[PtCl_4]$							
Experimental	5420	−4990	−4990	−1520	10 410	−1.00	-
Third (VMTA/BV)	4714	−4681	−4681	−1549	9395	−1.00	304
First (VMTA/BV)	11 365	−3243	−3243	1626	14 608	−1.00	3386
First (Standard)	5746	−4258	−4259	−924	10 005	−1.00	608
PtS							
Experimental	4023	−3734	−5920	−1877	9943	−0.56	-
Third (VMTA/BV)	2829	−4137	−5774	−2361	8603	−0.62	596
First (VMTA/BV)	10 490	−3337	−3416	1245	13 906	−0.99	3505
First (Standard)	−2128	−7506	−8734	−6122	6606	−0.63	4337

[a]Calculations of ^{195}Pt magnetic shielding were performed at the PBE0/SO level.

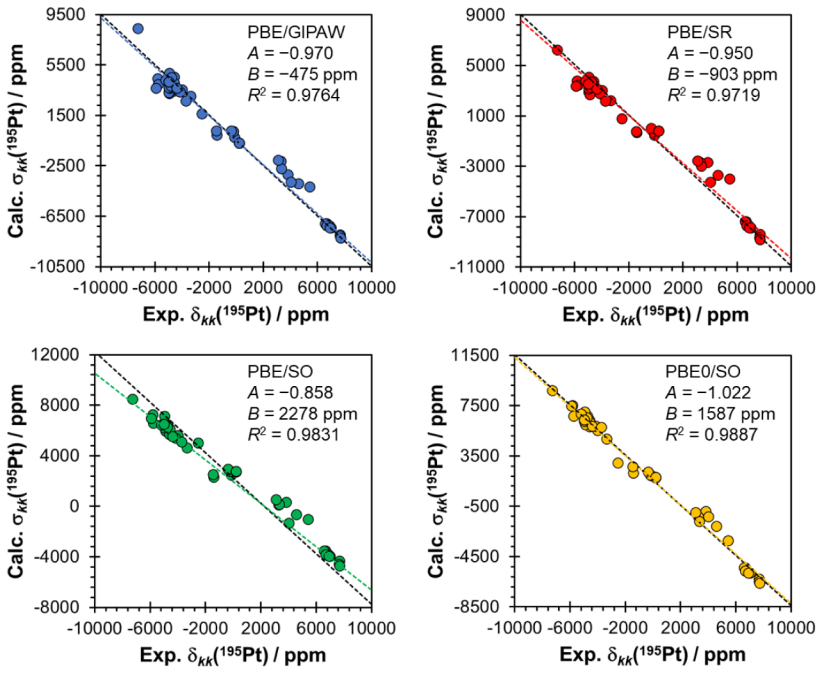

Figure 1. Correlations between calculated principal components of ^{195}Pt magnetic shielding tensors and experimental ^{195}Pt chemical shift tensors, as determined using different computational protocols. Computed shielding constants were obtained using PBE/GIPAW (blue), PBE/SR (red), PBE/SO (green), and PBE0/SO (yellow) methods. Colored lines represent the best-fit line in which the parameters A and B are optimized to minimize the value of Δ_{RMS} (see eqs 2−5). The black lines are fits constrained to an ideal slope of −1.

intermolecular interactions through the inclusion of the complete first coordination shell of molecules. For cisplatin, the small cluster consists of a central molecule as well as two molecules for which the intermolecular Pt−Pt contact distances are *ca.* 3.4 Å, whereas the medium cluster also includes six molecules featuring Pt−Cl and/or Pt−NH_3 contacts. For transplatin, the small cluster consists of a central molecule as well as two molecules featuring Pt−NH_3 contacts of *ca.* 3.6 Å, whereas the medium cluster also includes four molecules with Pt−Cl and Pt−NH_3 contacts up to *ca.* 4.7 Å. In contrast, the large clusters of cisplatin and transplatin both consist of the 15 molecules that comprise the first complete molecular coordination shell (Scheme 1).

Intermolecular effects on ^{195}Pt magnetic shielding tensors are significant, with variation dependent on the nature of the intermolecular interactions (Table 1). We note several observations: (i) inclusion of additional molecules in the cluster typically results in an increase in the span of the magnetic shielding tensor, leading to better agreement with experiment; (ii) for cisplatin, intermolecular interactions have the greatest effect on δ_{11}, the least shielded principal component oriented perpendicular to the L_4Pt plane, which is deshielded by 806 ppm in the full cluster model relative to the isolated molecule, reflecting the sensitivity of out-of-plane orbitals to the surrounding environment; (iii) for transplatin, intermolecular effects influence all three principal components of the magnetic shielding tensor, resulting in either shielding or deshielding depending on the size of the cluster; and (iv) increasing the size of the cluster beyond the first complete coordination shell of molecules is very costly and has little effect on the computed magnetic shielding tensor. The importance of intermolecular effects on the ^{195}Pt magnetic shielding tensors is evaluated for 10 molecular solids in Figure S1. These calculations have associated errors (relative to experiment) of Δ_{RMS} = 391 and 580 ppm for clusters and isolated molecules, respectively. From these results, it is evident that calculations on clusters that include the complete first coordination shell of molecules represent the best trade-off between computational cost and accuracy. The origins

https://doi.org/10.1021/acs.inorgchem.5c05169
Inorg. Chem. 2026, 65, 4430−4445

of the intermolecular effects on magnetic shielding tensors differ for cisplatin and transplatin, which are discussed in detail in Section 3.3.

3.2.2. Ionic and Network Solids. The utility of the VMTA/BV model (Scheme 2) for calculations on ionic and/or network solids is illustrated through a comparison of calculations on clusters in which the pseudoatom model is employed and clusters in which it is not (i.e., an "untreated" cluster); for the latter case, large net charges result due to the missing coordination counterions (Figure S2). For this comparison, we use third-coordination shell clusters of all six network solids. The untreated clusters have net charges that range between −18 and −64 depending on the system. Use of the VMTA/BV cluster model resulted in SCF convergence in less than 20 cycles for all systems, whereas use of the untreated clusters resulted in SCF convergence for only two systems after 300 cycles.

We next examined the effects of cluster size on the calculation of ^{195}Pt magnetic shielding tensors for clusters that are constructed to include up to the first, third, or fifth coordination shells of atoms. Additionally, we examined the use of first coordination shell clusters with standard nuclear charges, since SCF convergence is possible for these. Calculations using first coordination shell clusters, whether using standard or VMTA/BV nuclear charges, are insufficiently large to model the effects of the local environment on magnetic shielding tensors, based on the poor agreement with experiment (Table 2, Figure S3). Calculations using fifth coordination shell clusters are very costly due to the large number of Pt atoms and could not be completed for any system. Consistent with previous work using this approach,[59,122] calculations on third coordination shell clusters with VMTA/BV charges result in good agreement with experiment and are consequently used in the analyses in Section 3.3.

3.3. Survey of ^{195}Pt Magnetic Shielding Tensors

Here, we evaluate calculations of the ^{195}Pt magnetic shielding tensors for 16 solids, including ten molecular solids and six network solids. The relationships between the principal components of the experimental chemical shift tensors and calculated magnetic shielding tensors are shown in Figure 1. Statistical analysis associated with these calculations is displayed in Table 3, a summary of the best calculations is in Table 4 (*vide infra*), and a listing of all calculated values is given in Table S4.

First, we compare two methods of calculating ^{195}Pt magnetic shielding tensors: (i) PBE/GIPAW calculations (plane wave basis sets and SR pseudopotentials generated on-the-fly) and (ii) PBE/SR calculations performed with cluster-based models (GIAO formalism, all-electron Slater-type basis functions, and the ZORA/SR Hamiltonian). The key difference between these two sets of calculations is that the former accounts for intermolecular interactions through the use of periodic boundary conditions, whereas the latter uses clusters of atoms or molecules (depending on the nature of the system). Cluster models for the molecular solids consist of 9−15 molecules, whereas those of the network solids are composed of all atoms up to the third coordination shell. Both methods accurately model intermolecular effects on the magnetic shielding tensors, resulting in correlation lines with slopes that deviate slightly from the ideal of −1 (Table 3). For instance, PBE/GIPAW and PBE/SR calculations yield A = −0.970 and −0.950, respectively, with comparatively similar intercepts of B = −475 and −903 ppm, respectively. Furthermore, the RMS chemical shift distances for the PBE/GIPAW and PBE/SR calculations are Δ_{RMS} = 525 and 607 ppm, respectively.

Second, we explore the importance of SO interactions on the computed magnetic shielding tensors (i.e., PBE/SR vs. PBE/SO). SO effects have a large impact on the calculated values of ^{195}Pt magnetic shielding tensors, which is most apparent in the intercept of the correlation line (B = 2278 ppm) and the slope (A = −0.858), the latter of which deviates substantially from the ideal value of −1. The use of the ZORA/SO Hamiltonian results in increased shielding of the reference by *ca.* 3200 ppm relative to the value predicted at the PBE/SR level, which is consistent with previous calculations on the shielding of sixth-period elements[58,59] (*N.B.:* these differences tend to be an order of magnitude smaller for fifth-period elements such as Cd, Sn, Te, and Rh).[53,56,57,59,121]

Third, the use of the hybrid functional PBE0 in combination with the ZORA/SO Hamiltonian (i.e., PBE0/SO), leads to the best agreement with experimental ^{195}Pt chemical shift tensors. The use of the PBE0 functional results in changes to the individual principal components of the ^{195}Pt magnetic shielding tensors that differ in magnitude and direction relative to calculations performed at the PBE/SO level; this results in a correlation line with a slope much closer to −1 (A = −1.022), as well as a decrease in the total shielding of the reference compound (B = 1587 ppm). Most significantly, these calculations result in excellent agreement with experiment, as characterized by Δ_{RMS} = 374 ppm, which corresponds to *ca.* 2.5% of the ^{195}Pt chemical shift range of *ca.* 15 000 ppm. This observation, that the combination of hybrid functionals and relativistic effects at the SO level provides the best agreement with experiment, is consistent with previous studies of the magnetic shielding of fifth- and sixth-period nuclides.[53,56,57,59,121] The differences in the performance of the PBE and PBE0 functionals likely relates at least in part to the electron delocalization error (DLE),[126] a well-known phenomenon in Kohn−Sham DFT that results from spurious self-repulsion of electrons, the effects of which vary with the functional approximations used, as well as the system under consideration. The reason why the DLE is important in the context of NMR of transition metal complexes is that it impacts the extent of dative bonding because the latter is a delocalization phenomenon. The inclusion of an admixture of exact exchange in hybrid functionals (e.g., 25% in the standard PBE0 approximation) often greatly alleviates the DLE, and as in the present case, provides more accurate predictions of ^{195}Pt magnetic shielding tensors. This is evidenced by the consideration of the PBE0/SO calculations for all of the systems herein, as compared in Table 4.

Table 3. Statistical Analysis Related to the Correlation between Calculated ^{195}Pt Magnetic Shielding Tensors and ^{195}Pt Experimental Chemical Shift Tensors[a]

	N	A	B (ppm)	Δ_{RMS} (ppm)
GIPAW	16	−475	−0.970	525
PBE/SR	16	−903	−0.950	607
PBE/SO	16	2278	−0.858	508
PBE0/SO	16	1587	−1.022	374

[a]The parameters N, A, B, and Δ_{RMS} refer to the number of Pt sites (N), the interpolated magnetic shielding of the reference state (B), the slope of the correlation line (A), and the RMS chemical shift difference (Δ_{RMS}). See eqs 2−5 for definitions.

https://doi.org/10.1021/acs.inorgchem.5c05169
Inorg. Chem. 2026, 65, 4430−4445

Table 4. Experimental and Calculated (PBE0/SO) ^{195}Pt Chemical Shift Tensors[abc]

Material		δ_{11} (ppm)	δ_{22} (ppm)	δ_{33} (ppm)	δ_{iso} (ppm)	Ω (ppm)	κ	d_ν (ppm)
cis-$PtCl_2(NH_3)_2$	Exp.[29]	4100	−4697	−4877	−1825	8977	−0.96	-
	Calc.	2428	−4147	−5003	−2241	7431	−0.77	624
trans-$PtCl_2(NH_3)_2$	Exp.[29]	3260	−4020	−5840	−2200	9100	−0.60	-
	Calc.	2837	−3848	−5811	−2274	8648	−0.55	185
$Pt(cbdca)(NH_3)_2$	Exp.[29]	4576	−4927	−4974	−1775	9550	−0.99	-
	Calc.	3577	−4798	−4868	−2030	8445	−0.98	419
$PtCl_2(en)$	Exp.[29]	3342	−4900	−4983	−2180	8325	−0.98	-
	Calc.	3203	−4326	−4568	−1897	7771	−0.94	343
$Pt[S_2P(OEt)_2]_2$	Exp.[28]	−2530	−4608	−4953	−4030	2423	−0.72	-
	Calc.	−1323	−4652	−5317	−3764	3994	−0.67	505
$PtCl_2(MeCN)_2$	Exp.[39]	3090	−4831	−5760	−2500	8850	−0.79	-
	Calc.	2515	−4843	−4996	−2441	7511	−0.96	352
$Pt(dmpe)Me_2$	Exp.[19]	−4146	−4587	−4776	−4503	630	−0.40	-
	Calc.	−4199	−4542	−4875	−4539	676	−0.01	52
$PtCl_4(NH_3)_2$	Exp.[22]	−134	−209	−367	−237	233	0.36	-
	Calc.	−370	−386	−623	−460	253	0.87	224
$Pt(tfd)_2$	Exp.[24]	−1427	−3357	−7277	−4020	5850	0.34	-
	Calc.	−546	−3193	−6983	−3574	6437	0.18	488
$[Pt(tfd)_2][NEt_4]_2$	Exp.[21]	−1468	−4389	−5213	−3690	3745	−0.56	-
	Calc.	−1051	−4200	−5140	−3464	4089	−0.54	244
$K_2[PtCl_4]$	Exp.[30]	5429	−4990	−4990	−1517	10 419	−1.00	-
	Calc.	4714	−4681	−4681	−1549	9395	−1.00	304
$K_2[PtCl_6]$	Exp.[30]	207	207	207	207	0	n/a	-
	Calc.	−204	−209	−212	−208	8	−0.25	416
PtS	Exp.[32,33]	4023	−3734	−5920	−1877	9943	−0.56	-
	Calc.	2829	−4137	−5774	−2361	8603	−0.62	596
$K_2[PtF_6]$	Exp.[31]	7683	6673	6578	6978	1105	−0.83	-
	Calc.	7673	6795	6792	7087	881	−0.99	123
$Rb_2[PtF_6]$	Exp.[31]	7657	6871	6685	7071	972	−0.62	-
	Calc.	7882	7081	7078	7347	804	−0.99	281
$Cs_2[PtF_6]$	Exp.[31]	7700	6998	6908	7202	792	−0.77	-
	Calc.	8016	7209	7205	7477	811	−0.99	276

[a]The following abbreviations are used in compound names: cbdca = cyclobutanedicarboxylic acid; en = ethylenediamine; dmpe = 1,2-bis(dimethylphosphino)ethane; tfd = $S_2C_2(CF_3)_2$. [b]Calculations were performed at the PBE0/SO level with clusters used to model the crystal lattice, as detailed in the text. [c]Calculated ^{195}Pt magnetic shielding tensors were converted to the chemical shift scale using eqs 3−5 and the values in Table 3.

Scheme 3. Illustration of the Orbital "Rotation" Model for $[PtCl_4]^{2-}$[a]

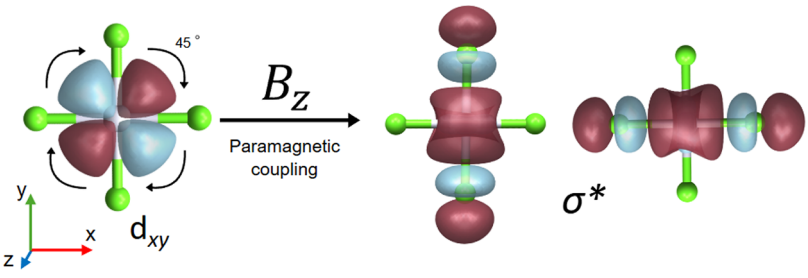

[a]In this example, an external field along the *z*-axis causes a 45° rotation of the occupied NB d_{xy} lone pair orbital, which can then couple with the unoccupied σ* orbitals of the correct symmetry.

3.4. Localized Orbital Analysis of ^{195}Pt Magnetic Shielding Tensors

3.4.1. Overview. An orbital "rotation" model[127] for the Pt 5d shell, combined with a localized orbital analysis from SO relativistic DFT calculations, is a powerful tool for analyzing trends in the highly variable chemical shift tensors of Pt coordination compounds.[12,13,25,53] This method rationalizes the origins of contributions to the shielding in terms of magnetic coupling of occupied orbitals with unoccupied orbitals of the proper local symmetry.

The d-atomic orbital (AO) "rotation" model setup[12] is as follows (Scheme 3): The first-order perturbation of a d-AO in the standard set (d_{xy}, d_{xz}, d_{yz}, $d_{x^2-y^2}$, d_{z^2}) by a static magnetic field along one of the Cartesian axes is proportional to the AO rotated by either 45° or 90°, depending on the orbital and field direction. A magnetic field aligned in the *z* direction causes no perturbation in d_{z^2} (to first order; minor contributions are

https://doi.org/10.1021/acs.inorgchem.5c05169
Inorg. Chem. 2026, 65, 4430−4445

Table 5. NLMO Analysis of Isotropic Pt Shielding for a Set of Isolated Molecules[a,b,c]

	$[PtF_6]^{2-}$	$[PtCl_4]^{2-}$	$[PtCl_6]^{2-}$	Cisplatin	Transplatin	$PtCl_4(NH_3)_2$	$Pt(cbdca)(NH_3)_2$	$Pt(dmpe)Me_2$
Pt core	13 653	12 793	12 299	12 288	12 438	12314	12 328	12 156
$LP(Pt)_a$	−5340	137	−2966	−622	−1157	−2826	−1730	−462
$LP(Pt)_b$	−5883	−1627	−2967	−910	−1	−2834	−1548	−842
$LP(Pt)_c$	−5882	−1626	−2967	−1243	−1730	−2987	−533	−714
$LP(Pt)_d$		−4951		−3465	−3849		−3339	−1211
∑Pt LP	−17 106	−8068	−8899	−6238	−6738	−8647	−7151	−3229
σ(Pt−X)[d]	−2207	−1778	−1329	−858	−1009	−995	−724	−1329
σ(Pt−Y)[d]				−724	−599	−392	−651	−1055
$\sum\sigma$(Pt−L)[d]	−2207	−1778	−1329	−1582	−1608	−1387	−1375	−2385
L core	0	0	1	1	1	1	2	5
L LP	−323	−81	106	73	31	236	−93	
SO unocc[e]	−165	−336	−356	−371	−346	−369	−227	−592
Total	−6148	2531	1821	4171	3783	2148	3484	6165

[a]Isolated molecular structures were extracted from the refined crystal structures. [b]In the NLMO analysis, the SO and paramagnetic contributions are combined into a single term, whereas purely paramagnetic (non-SO) effects can be obtained separately by running the analysis with only SR effects taken into account. [c]NLMOs listed as LP are nonbonding. [d]Includes contributions from NLMOs with bonding and LP parent NBOs, which are fully σ-bonding. L denotes ligands. Depending on the complex, X may be Cl, F, O, S, or P and Y may be N or C. [e]Shielding contributions arise from SO-induced mixing of unoccupied SR MOs into the SO−DFT ground state.

obtained at the relativistic level).[128] However, if the field is applied to a nonbonding occupied [lone pair (LP)] 5d AO, and the magnetically induced "rotation" results in significant overlap with a low-energy unoccupied molecular orbital (MO) (e.g., a σ^* paired with a dative σ bonding orbital from a coordinating ligand), the result is deshielding of the nucleus by the occupied 5d AO and its magnetic coupling with the σ^*. The well-known perturbation theory formulas apply here,[12] such that the deshielding effect is large if (i) the 5d AO and the σ^* MO are close in energy and (ii) σ^* has significant overlap with the "rotated" 5d AO. All subsequent NLMO-based shielding analyses are performed at the PBE0/SO level because these calculations lead to the best agreement with experiment (Section 3.3).

3.4.2. Trends in Isotropic Magnetic Shielding. Table 5 summarizes the results of the NLMO analysis of the absolute isotropic shielding for a representative set of isolated Pt complexes. As expected, the largest contribution to the total shielding is from the Pt core, albeit with relatively minor variation between systems. The primary differences in isotropic shielding arise from the deshielding caused by the Pt LP 5d AOs, as well as valence ligand orbitals that donate electron density to the formally unoccupied Pt 5d shell.

The trends for 4-coordinate vs 6-coordinate Pt are exemplified by the comparison between $[PtCl_6]^{2-}$ and $[PtCl_4]^{2-}$, which feature $5d^6$ and $5d^8$ formal configurations, respectively (*cf.* Figures S4 and S5 for pictures of key nonbonding 5d and σ bonding/antibonding NLMOs in $[PtCl_6]^{2-}$ and $[PtCl_4]^{2-}$, respectively). For $[PtCl_6]^{2-}$, the Pt−Cl bonds are oriented along the Cartesian axes and the three occupied Pt 5d LPs are described as d_{xy}, d_{xz}, and d_{yz}, which are equivalent (i.e., $LP(Pt)_c$, $LP(Pt)_a$, and $LP(Pt)_b$, respectively). If the magnetic field is perpendicular to the plane of any one of these AOs, then the first-order magnetically induced perturbation corresponds to a 45° in-plane "rotation" that causes their lobes to align with four Pt−Cl bonds. The magnetically induced coupling generated by the overlap of the "rotated" 5d AO with the σ^* MOs that are paired with the σ donation bonds from the chlorine ligands (e.g., $d_{xy} - \sigma_a^*$ and $d_{xy} - \sigma_b^*$ mixing, see Figure S4) causes large deshielding contributions parallel to the magnetic field (*ca.* −3000 ppm per LP, Table 5). For $[PtCl_4]^{2-}$, the situation is different (Figure S5). First, there is one additional occupied 5d LP, namely $5d_{z^2}$ (i.e., $LP(Pt)_a$); however, it has a negligible contribution to shielding in comparison to that of the other 5d LPs. Second, for the ligands in the *xy* plane, a magnetic field in the *z* direction creates a 45° "rotation" of d_{xy}, resulting in overlap of all lobes with σ^* orbitals; this magnetically induced $LP(Pt)_d - \sigma_a^*$ and $LP(Pt)_d - \sigma_b^*$ mixing results in isotropic deshielding of *ca.* −4951 ppm. Third, d_{xz} ($LP(Pt)_b$) and d_{yz} ($LP(Pt)_c$), which are not equivalent to d_{xy} ($LP(Pt)_d$), undergo mixing with σ^* MOs, though to a lesser degree than those in the octahedral $[PtCl_6]^{2-}$. This is mostly caused by the absence of σ^* MOs in the *z* direction in $[PtCl_4]^{2-}$, which diminishes the induced magnetic coupling, since only two of the lobes of the "rotated" AOs overlap with antibonding σ^* MOs (instead of all four lobes in the case of d_{xy}).

Similar trends are observed in the NLMO analyses for $PtCl_4(NH_3)_2$, cisplatin, transplatin, and $Pt(cbdca)(NH_3)_2$, the first of which has a $5d^6$ formal configuration, and the latter three have a $5d^8$ configuration. Pt isotropic shielding for $PtCl_4(NH_3)_2$, like $[PtCl_6]^{2-}$, largely arises from the occupied Pt 5d LPs (i.e., d_{xy}, d_{xz}, and d_{yz} or $LP(Pt)_c$, $LP(Pt)_a$, and $LP(Pt)_b$), though in this case, the contributions are not identical due to the presence of both Pt−Cl and Pt−N covalent bonds (Figure S6). For the three planar compounds, a major deshielding contribution arises from the d_{xy} LP orbital ($LP(Pt)_d$ (Figures S7−S9), albeit a smaller contribution than in $[PtCl_4]^{2-}$, due to differences in degrees of overlap and energies between the coupled bonding and antibonding orbitals in each system.

We next examine the striking difference between the ^{195}Pt chemical shifts of $K_2[PtF_6]$ (Figure S10) and $K_2[PtCl_6]$ (Figure S4), which have the same octahedral Pt−halide bonding motif and formal metal oxidation state. The difference in shielding largely results from the three 5d LPs, i.e., the t_{2g} set of d orbitals. The combined contribution is over −17 000 ppm in $[PtF_6]^{2-}$, whereas it is only *ca.* −8000 ppm in $[PtCl_6]^{2-}$. This large disparity reflects differences in Pt−ligand bonding, as the more ionic Pt−F bonds lead to greater localization of the 5d lone pairs and hence stronger deshielding contributions than the more covalent Pt−Cl bonds (*vide infra*).

This made us wonder what the shielding of a Pt^{IV} ion in a $(t_{2g})^6$ configuration would be in a purely electrostatic crystal

https://doi.org/10.1021/acs.inorgchem.5c05169
Inorg. Chem. 2026, 65, 4430−4445

Table 6. Averaged Calculated Parameters for Relevant 3c4e NBO/NLMOs[a] of $K_2[PtF_6]$ and $K_2[PtCl_6]$

		NLMO			NBO	
	orbital type	% L[b]	% Pt[b]	% *trans*-L[b]	$E^{(2)}$/eV	NBO pop[c]
$K_2[PtF_6]$	$LP(F)_{a,b,c}$	83.6	13.1	3.1	5.03	1.69
	$\sigma(Pt-F)_{d,e,f}$	80.6	17.0	0	0.22	1.98
	$\sigma^*(Pt-F)_{a,b,c}$ (NBO)	18.2	81.8	–	–	0.34
$K_2[PtCl_6]$	$LP(Cl)_{a,b,c}$	73.9	17.2	8.5	7.24	1.49
	$\sigma(Pt-Cl)_{d,e,f}$	65.5	33.7	0.1	0.04	1.98
	$\sigma^*(Pt-Cl)_{a,b,c}$ (NBO)	33.0	67.0	–	–	0.52

[a]Optimized octahedral geometry has Pt−F distances of 1.991 Å. [b]The NLMOs corresponding to one of these "LP" NBOs are σ-bonding and labeled as $\sigma(Pt-F)^{LP}_{a,b,c}$ in Figure S4. The density weights in columns 3−5 are for the corresponding NLMOs. The $E^{(2)}$ data are for the primary NBO delocalization into the trans σ^* antibond. [c]Population of the parent NBO.

field, without any covalent bonding (Figure S11). To answer this question, a model calculation was set up for a Pt^{IV} ion in an octahedral field of point charges. Here, the t_{2g} 5d AOs strongly couple with the unoccupied e_g* AOs. For point charges of −1 au placed at the distance for an isolated $[PtF_6]^{2-}$ complex (1.965 Å), the isotropic shielding contribution from the Pt LPs is on the order of -8×10^5 ppm, with a $t_{2g} - e_g$* orbital energy gap of about 4.5 eV. Using point charges of −2 au, the energy gap increases to 5.0 eV, while the isotropic shielding contribution decreases in magnitude to -2×10^5 ppm (i.e., the deshielding is reduced). Although these purely ionic electronic structures will not be present in any real complex where there is always some degree of covalency, the model calculations demonstrate that in the limit of vanishing covalency, the paramagnetic deshielding originating from a closed-shell $(t_{2g})^6$ 5d shell in an octahedral crystal field is strongly amplified.

The underlying reason for this can be seen in the form of the paramagnetic nuclear-spin electron-orbital (PSO) quantum operator underlying the paramagnetic deshielding, which is (nonrelativistically) proportional to $(r^{-3})\mathbf{r} \times \nabla$, with vector $\mathbf{r}$ of length r being the position of an electron relative to the Pt nucleus. The resulting shielding contributions are therefore very sensitive to how strongly the magnetically coupled occupied and unoccupied orbitals are localized on the Pt atom, as well as to the $t_{2g} - e_g$* energetic splitting. Evidently, the complexes and network solids investigated herein are far departed from a hypothetical purely ionic limit.

Table 6 provides a more detailed analysis of key bonding orbitals in $[PtF_6]^{2-}$ and $[PtCl_6]^{2-}$. These results were obtained from optimized structures with idealized octahedral geometries (rather than the optimized crystal structure geometries used elsewhere). These systems feature 3-center 4-electron (3c4e) ligand (L)−metal (M) bonds *trans* across the metal center as follows:

$$L: \quad M-L \leftrightarrow L-M \quad :L$$

The NBO program typically produces one of the resonance structures for such a bond, as exemplified by the selected orbitals for $[PtCl_6]^{2-}$ (Figure 2). For each *trans* L−M−L set, the localization analysis yields one ligand LP with σ symmetry, and a corresponding *trans* σ-bonding orbital accompanied by a σ* antibond, where the LP designation only applies to the corresponding "parent" NBO of the LP. The corresponding NLMO has significant bonding and 3-center character and appears similar to the *trans* bonding NLMO (*N.B.*: even though the delocalized LPs and the bond orbitals are not identical, this does not indicate a breaking of the octahedral symmetry).

The orbitals in Table 6 are classified as three M−L bonds (second row) and three corresponding ligand LPs (first row).

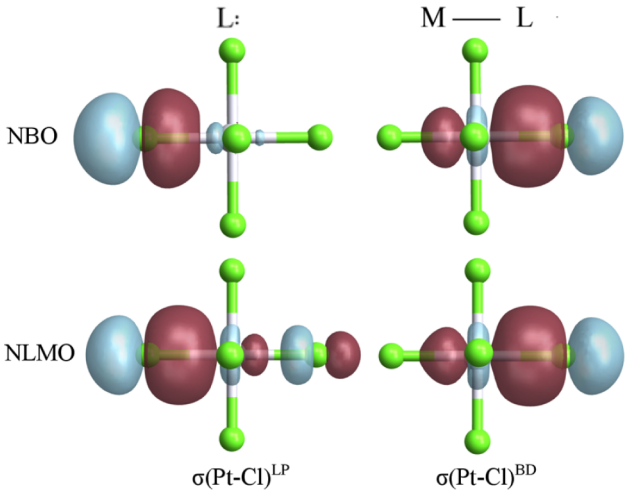

Figure 2. NBO vs NLMO representation of the orbital pair representing one of the 3c4e bonds in $[PtCl_6]^{2-}$.

These data quantify the extents of covalency and delocalization in several ways. Reported for each group of symmetry-equivalent orbitals are the average percent density weights of the NLMOs on each atomic center involved in the L−Pt−L interaction. Clearly, the Pt weights are considerably larger for Cl than for F. The ligand "LP" NBO also has a much larger delocalization energy, $E^{(2)}$, for Cl as compared to F, and a stronger 3c character as evidenced by the larger weight of the resulting NLMO on the *trans* ligand. The magnitude of $E^{(2)}$ correlates with the population of the LP NBO falling much below 2 as it delocalizes to form a 3c bonding NLMO, which goes along with a corresponding nonzero population of the *trans* σ* antibond. In a comparison of $[PtCl_6]^{2-}$ and $[PtF_6]^{2-}$, the NBO populations of the $[PtCl_6]^{2-}$ LP are lower, and the *trans* σ* NBO populations are higher. As a result of the higher covalency of Pt−Cl bonds, the paramagnetic deshielding from the nonbonding 5d AOs has a much smaller magnitude, as the relevant orbitals become delocalized toward the ligands.

Another way of stating the results from the analysis of $K_2[PtCl_6]$ and $K_2[PtF_6]$ is the following: In a hypothetical $(t_{2g})^6$ ion in a crystal field, without bonding, there is a huge paramagnetic coupling of the 5d nonbonding t_{2g} AOs with the unoccupied e_g* AOs. Covalency via dative σ bonding puts electron density into the e_g* AOs, which are therefore no longer fully available for magnetic coupling. The empty e_g* AOs are L−M antibonding and, therefore, not fully localized on Pt. As a consequence, the deshielding contributions from the 5d AOs are strongly reduced with increasing Pt−X covalency.

https://doi.org/10.1021/acs.inorgchem.5c05169
Inorg. Chem. 2026, 65, 4430−4445

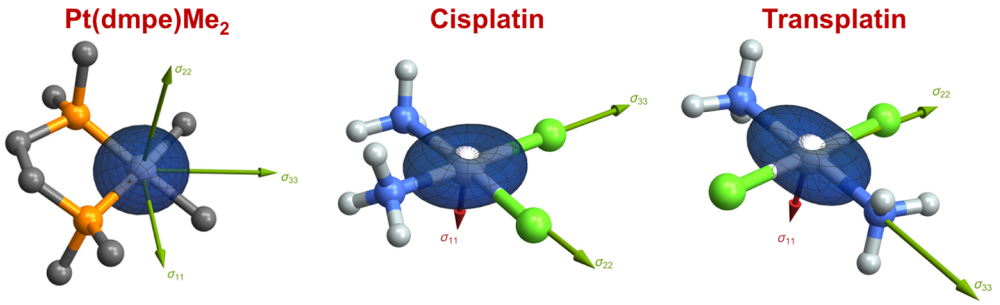

Figure 3. Polar plots of the total calculated shielding tensor and the corresponding principal components superimposed on the molecules Pt(dmpe)Me_2, cisplatin, and transplatin. The lengths of the vectors indicate the principal components, which are not drawn to scale but are scaled relative to each other to convey the magnitude pattern for the principal components. Some hydrogen atoms have been removed for clarity.

For comparison, Table S5 summarizes the results of the NLMO analysis of the isotropic shielding for a representative set of Pt complexes, with cluster models used to represent their respective lattice environments. A more detailed discussion of the role of intermolecular effects on magnetic shielding tensors is discussed below.

3.4.3. Trends in Magnetic Shielding Tensors. The principal components of the shielding tensor can also be decomposed into NLMO contributions. We discuss the interesting case of Pt(dmpe)Me_2, which features an unusually small span for a Pt^{II} complex (Ω = 630 ppm),[19] as well as the importance of stereochemical and intermolecular effects on the ^{195}Pt magnetic shielding tensors of cisplatin and transplatin. The latter comparison was prompted by the markedly smaller span of cisplatin (Ω = 8561 ppm) in comparison to that of transplatin (Ω = 9100 ppm).[29] Graphical representations of the total shielding tensors in the form of polar plots[129] and their principal axis systems are shown in Figure 3.

The very low chemical shift (indicating a shielded ^{195}Pt nucleus) and small chemical shift span of Pt(dmpe)Me_2 in comparison to the other molecular Pt^{II} complexes is unexpected (Table 7), given that it has a Pt d^8 formal configuration and an almost planar ligand field. Using labels as defined in Figure S12, we expect higher deshielding in component σ_{22} (perpendicular to the Pt−ligand plane), particularly from the in-plane LP(Pt)$_d$ AO, because of the expected overlap with the σ^* MO upon 45° "rotation". The comparatively small magnitude of this contribution is attributed to a reduced electron population of the corresponding LP(Pt)$_d$ parent NBO due to back-bonding from the Pt center to the σ^*(C−P) MO, which is clearly visible in the NLMO isosurfaces (σ(Pt−C)$_c^{BD}$ and σ(Pt−C)$_d^{BD}$ in Figure S12). Similar back-bonding takes place via LP(Pt)$_b$ and LP(Pt)$_c$; the populations of the parent NBOs are calculated to be 1.9 in the isolated complex, indicating back-donation of the equivalent of 0.1 electrons each.

Table 7. Calculated NLMO Contributions to the Principal Components of the ^{195}Pt Magnetic Shielding Tensor of Pt(dpme)Me_2

	σ_{11} (ppm)	σ_{22} (ppm)	σ_{33} (ppm)
Pt core	12 555	11 185	12 729
LP(Pt)$_a$	−971	−1	−416
LP(Pt)$_b$	−816	−554	−1156
LP(Pt)$_c$	−726	−2583	−324
LP(Pt)$_d$	−821	−680	−640
∑Pt LP	−3335	−3818	−2535
σ(Pt−P)	−1884	−330	−1774
σ(Pt−C)	−1089	−659	−1418
∑above	6247	6378	7002
Total calc.	5716	6289	6489

The major contributions to the shielding tensor are similar for cisplatin and transplatin. The Pt LP NLMOs (Figures S7 and S8, respectively) more closely resemble the canonical d set in the case of transplatin; therefore, we use this complex as an example for our analysis. LP(Pt)$_a$ (i.e., the d_{xz}) generates a large deshielding in σ_{33} because a static magnetic field along the N−Pt−N bond axis rotates two of the lobes of the d_{xz} into an orientation to overlap with the σ^*(Pt−Cl) orbitals. LP(Pt)$_c$ (i.e., d_{yz}) is rotated to overlap with the σ^*(Pt−N) orbitals by a field in the σ_{22} direction, creating a slightly larger deshielding effect. Finally, the largest deshielding contribution from the d shell originates from in-plane LP(Pt)$_d$ (d_{xy}), which is rotated by a field in the σ_{11} direction such that all four lobes overlap with σ^* orbitals.

The primary reason for the narrower span for cisplatin is a reduced magnitude of σ_{11} in cisplatin by 1268 ppm as compared to that in transplatin (Tables 8 and 9). This represents the principal component perpendicular to the molecular plane, the magnitude of which is determined by paramagnetic coupling of the in-plane Pt d_{xy} orbital with unoccupied σ^* orbitals. This coupling, which can be affected by factors such as degree of spatial overlap, donation vs back-donation, as well as relative energies of the coupling orbitals, is stronger in transplatin than cisplatin. Transplatin has a $d_{xy} - \sigma^*$(Pt−Cl) energy gap that is smaller than that of cisplatin by 0.49−1.0 eV, depending on which of the two calculated cisplatin σ^*(Pt−Cl) NBOs are considered; this has an enhancing effect on the coupling in the former within the usual interpretation of the shielding in terms of orbital energy gaps and magnetic coupling matrix elements.

The ^{195}Pt magnetic shielding tensors of cisplatin and transplatin are also affected by intermolecular interactions (Tables 8 and 9). In cisplatin, a weak interaction occurs between stacked d_{z^2}-like Pt orbitals (Figure S13), effectively acting as a weak axial ligand, resulting in additional paramagnetic deshielding arising from the Pt d-shell, as well as from the σ(Pt−Cl) and σ^*(Pt−N) orbitals; this is most evident in the unique principal component, σ_{11}, which lies perpendicular to the plane of the molecule. For transplatin, intermolecular interactions influence σ_{22} and σ_{33}. The bulk of this effect originates from relatively minor changes to contributions from the Pt 5d shell, as well as the Pt−ligand bonding orbitals. Therefore, the effect is not from the lattice directly, but rather from the influence of the lattice on the orbitals of the central molecule in the cluster. Unlike cisplatin, which affords Pt−Pt

https://doi.org/10.1021/acs.inorgchem.5c05169
Inorg. Chem. 2026, 65, 4430−4445

Table 8. NLMO Analysis of Isotropic Pt Shielding for Cisplatin as an Isolated Molecule and a Molecule in a Cluster[abc]

	Isolated Molecule			Cluster		
	σ_{11} (ppm)	σ_{22} (ppm)	σ_{33} (ppm)	σ_{11} (ppm)	σ_{22} (ppm)	σ_{33} (ppm)
Pt core	11 908	12 425	12 530	11 907	12 223	12 314
$LP(Pt)_a$	14	−306	−1577	84	−390	−69
$LP(Pt)_b$	90	−515	−2300	29	−97	−3825
$LP(Pt)_c$	78	−3682	−122	89	−3996	−70
$LP(Pt)_d$	−10 313	−42	−34	−11 185	−42	−54
∑Pt LP	−10 131	−4544	−4033	−10 982	−4524	−4017
∑σ(Pt−Cl)	−823	−867	−884	−570	−859	−799
∑σ(Pt−N)	−563	−917	−694	−762	−685	−517
SO unocc.[d]	−507	−385	−220	−498	−356	−243
Direct lattice[e]	n/a	n/a	n/a	14	−95	−154
∑above	392	6098	6920	−961	5847	6722
Total calc.	−104	5811	6814	−961	5847	6722

[a]Cluster models representing the solids were constructed as explained in the text. [b]In the NLMO analysis, the SO and paramagnetic contributions are combined into a single term, whereas purely paramagnetic (non-SO) effects can be obtained separately by running the analysis with only SR effects taken into account. [c]NLMOs listed as LP are nonbonding. NLMOs listed as LP are nonbonding. [d]Shielding contributions from spin−orbit induced mixing of unoccupied scalar relativistic MOs into the SO−DFT ground state. [e]"Lattice effects" only include direct contributions from NLMOs centered on atoms other than the central complex.

Table 9. NLMO Analysis of Isotropic Pt Shielding for Transplatin as an Isolated Molecule and a Molecule in a Cluster[abc]

	Isolated Molecule			Cluster		
	σ_{11} (ppm)	σ_{22} (ppm)	σ_{33} (ppm)	σ_{11} (ppm)	σ_{22} (ppm)	σ_{33} (ppm)
Pt core	12 136	12 467	12 712	12 117	12 467	12 653
$LP(Pt)_a$	186	−97	−3560	155	−231	−3354
$LP(Pt)_b$	−130	−89	214	−911	−837	369
$LP(Pt)_c$	120	−5214	−97	88	−3947	−224
$LP(Pt)_d$	−11 549	38	−37	−10 626	−55	21
∑Pt LP	−11 373	−5362	−3479	−11 294	−5070	−3188
∑σ(Pt−Cl)	−992	169	−2203	−1194	46	−2003
∑σ(Pt−N)	−557	−1435	196	−374	−1715	285
SO unocc[d]	−530	−90	−418	−533	−318	−282
Direct lattice[e]	n/a	n/a	n/a	18	−28	−10
∑above	−1317	5748	6808	−1261	5382	7455
Total calc.	−1372	5850	6873	−1346	5515	7554

[a]Cluster models representing the solids were constructed as explained in the text. [b]In the NLMO analysis, the SO and paramagnetic contributions are combined into a single term, whereas purely paramagnetic (non-SO) effects can be obtained separately by running the analysis with only SR effects taken into account. [c]NLMOs listed as LP are nonbonding. NLMOs listed as LP are nonbonding. [d]Shielding contributions from spin−orbit induced mixing of unoccupied scalar relativistic MOs into the SO−DFT ground state. [e]"Lattice effects" only include direct contributions from NLMOs centered on atoms other than the central complex.

stacking in its crystal structure, the crystal structure of transplatin does not have close contacts between neighboring Pt centers; accordingly, no delocalization of orbitals is seen in the analysis of transplatin.

4. CONCLUSIONS

Quantum chemical calculations are essential for interpreting the relationships among ^{195}Pt chemical shift tensors, electronic structure, and Pt−ligand bonding. To achieve the best agreement between ^{195}Pt magnetic shielding tensors obtained from DFT computations and those from ^{195}Pt SSNMR measurements, we find that calculations must (i) include relativistic effects, including the SO interaction and the accompanying electron spin-dependent terms in the shielding tensor; (ii) be performed using a hybrid exchange-correlation functional such as PBE0; and (iii) in some cases, account for intermolecular interactions that impact ^{195}Pt chemical shifts using clusters of molecules to represent the crystal lattice. The PBE0/SO calculations result in excellent agreement with experiment, as characterized by Δ_{RMS} = 374 ppm, which corresponds to *ca.* 2.5% of the ^{195}Pt chemical shift range of *ca.* 15 000 ppm. Once this was established, it was possible to use NLMO and NBO analyses to interpret ^{195}Pt shielding tensors in terms of contributions from relevant bonding, antibonding, and nonbonding orbitals, providing insight into Pt−ligand interactions in terms of the metal- and ligand-centered bonds, lone pairs, and core−shells.

Crucial to applying this analysis to solids is the accurate modeling of the crystal lattice. To assess the accuracy of such models, a comparison between GIPAW and ADF/SR calculations is a good metric for both molecular and network solids. In this regard, software packages/codes such as *Abinit* may also prove useful. Further applications of periodic and/or cluster-based calculations find use across the Periodic Table and may be extended beyond bulk solids to systems such as immobilized and single-atom catalysts.[18,19,130−132]

The origins of chemical shift tensors can be analyzed in terms of contributions from relevant NLMOs and/or NBOs (or other

https://doi.org/10.1021/acs.inorgchem.5c05169
Inorg. Chem. 2026, 65, 4430−4445

sets of localized MOs), leading to an understanding of the electronic structure and chemical bonding in materials. Differences in shielding tensors among Pt coordination compounds are highly dependent on the Pt oxidation state and coordination environment, the magnitudes and orientations of paramagnetic shielding contributions arising from the Pt 5d shell, and the nature of orbitals originating from the ligand atoms having significant overlap with the Pt valence shells, energy gaps between key orbitals, and other factors such as intermolecular interactions. For instance, these analyses afford the quantification of the effects from ligand-to-metal donation and metal-to-ligand back-donation via the extent of delocalization of ligand/metal lone pairs onto the metal/ligand, which provides an intuitive picture of the effects of bonding on the metal magnetic shielding tensors.

Such analyses, when applied to the PGEs and ligands in coordination compounds, have the potential to revolutionize our understanding of structure−function-property relationships. This could lead to strategies not only for the rational design of novel catalysts and functional materials with tailored physicochemical properties and reactivities but also for the identification of new classes of analogous compounds using abundant and inexpensive replacement metals (e.g., Mn, Fe, Co, Ni, Cu) and novel classes of ligands. Furthermore, it is anticipated that these relativistic DFT methods and NBO/NLMO analyses will find applications (or have already found) in the analysis of other PGE complexes, including those of Rh, Ru, and Pd, as well as the atoms located in ligand atoms of coordination compounds via the study of relevant NMR-active nuclides.

■ ASSOCIATED CONTENT

Supporting Information

The Supporting Information is available free of charge at https://pubs.acs.org/doi/10.1021/acs.inorgchem.5c05169.

Crystallographic information; benchmarking calculations; additional NMLO analyses; summary of all calculated values; isosurface plots of all NLMOs; lists of atomic coordinates (PDF)

■ AUTHOR INFORMATION

Corresponding Authors

Robert W. Schurko − *Department of Chemistry & Biochemistry, The Florida State University, Tallahassee, Florida 32306, United States; National High Magnetic Field Laboratory, Tallahassee, Florida 32310, United States;* orcid.org/0000-0002-5093-400X; Email: rschurko@fsu.edu

Jochen Autschbach − *Department of Chemistry, University at Buffalo, State University of New York, Buffalo, New York 14260-3000, United States;* orcid.org/0000-0001-9392-877X; Email: jochena@buffalo.edu

Authors

Sean T. Holmes − *Department of Chemistry & Biochemistry, The Florida State University, Tallahassee, Florida 32306, United States; National High Magnetic Field Laboratory, Tallahassee, Florida 32310, United States;* orcid.org/0000-0002-5821-9641

Adam B. Philips − *Department of Chemistry, University at Buffalo, State University of New York, Buffalo, New York 14260-3000, United States;* orcid.org/0000-0002-5742-6817

Alberto Fernández-Alarcón − *Department of Chemistry, University at Buffalo, State University of New York, Buffalo, New York 14260-3000, United States*

Complete contact information is available at: https://pubs.acs.org/10.1021/acs.inorgchem.5c05169

Notes

The authors declare no competing financial interest.

■ ACKNOWLEDGMENTS

This material is based upon work supported by the U.S. Department of Energy, Office of Science, Office of Basic Energy Sciences, under Award Number DE-SC0022310. The authors are grateful for support from The Florida State University and the National High Magnetic Field Laboratory (NHMFL), which is funded by the National Science Foundation Cooperative Agreement (DMR-2128556) and the State of Florida. The authors also thank the Center for Computational Research (CCR) at the University at Buffalo for providing computing resources (http://hdl.handle.net/10477/79221).

■ REFERENCES

(1) Rao, C. R. M.; Reddi, G. S. Platinum group metals (PGM); occurrence, use and recent trends in their determination. *Trends Anal. Chem.* **2000**, *19*, 565−586.

(2) Hartley, F. R. *Chemistry of the Platinum Group Metals*; Elsevier Science Publishers B.V., 1991.

(3) ElGuindy, M. Platinum Group Metals: Alloying, Properties, and Applications. In *Encyclopedia of Materials: Science and Technology*; Buschow, K. H. J.; Cahn, R. W.; Flemings, M. C.; Ilschner, B.; Kramer, E. J.; Mahajan, S.; Veyssière, P., Eds.; Elsevier, 2001, pp. 7117−7121.

(4) *Critical Minerals and Materials - U.S. DOE's Strategy to Support Domestic Critical Mineral and Material Supply Chains (FY 2021−FY 2031)*; U. S. Department of Energy: Washington, D.C, 2020.

(5) *Mineral Commodity Summaries 2024*; U.S. Geological Survey: Reston, VA, 2024.

(6) Obeng, A.; Autschbach, J. How much electron donation is there in transition metal complexes? a computational study. *J. Chem. Theory Comput.* **2024**, *20*, 4965−4976.

(7) Hansen, J. H.; Parr, B. T.; Pelphrey, P.; Jin, Q.; Autschbach, J.; Davies, H. M. L. Rhodium(II)-catalyzed cross-coupling of diazo compounds. *Angew. Chem., Int. Ed.* **2011**, *50*, 2544−2548.

(8) Nassar, N. T. Limitations to elemental substitution as exemplified by the platinum-group metals. *Green Chem.* **2015**, *17*, 2226−2235.

(9) Graedel, T. E.; Harper, E. M.; Nassar, N. T.; Nuss, P.; Reck, B. K. Criticality of metals and metalloids. *Proc. Nat. Acad. Sci.* **2015**, *112*, 4257−4262.

(10) Widdifield, C. M.; Schurko, R. W. Understanding chemical shielding tensors using group theory, MO analysis, and modern density-functional theory. *Concepts Magn. Reson. Part A* **2009**, *34A*, 91−123.

(11) Fernández-Alarcón, A.; Autschbach, J. Relativistic density functional NMR tensors analyzed with spin-free localized molecular orbitals. *ChemPhysChem* **2023**, *24*, No. e202200667.

(12) Autschbach, J.; Zheng, S. Analyzing Pt chemical shifts calculated from relativistic density functional theory using localized orbitals: The role of Pt 5d lone pairs. *Magn. Reson. Chem.* **2008**, *46*, S45−S55.

(13) Autschbach, J. Analyzing NMR shielding tensors calculated with two-component relativistic methods using spin-free localized molecular orbitals. *J. Chem. Phys.* **2008**, *128* (16), 164112.

(14) Glendening, E. D.; Landis, C. R.; Weinhold, F. Natural bond orbital methods. *WIREs Comput. Mol. Sci.* **2012**, *2*, 1−42.

(15) Autschbach, J.; Zheng, S.; Schurko, R. W. Analysis of electric field gradient tensors at quadrupolar nuclei in common structural motifs. *Concepts Magn. Reson. Part A* **2010**, *36A*, 84−126.

(16) Sutter, K.; Autschbach, J. Computational study and molecular orbital analysis of NMR shielding, spin−spin coupling, and electric field gradients of azido platinum complexes. *J. Am. Chem. Soc.* **2012**, *134*, 13374−13385.
(17) Gordon, C. P.; Raynaud, C.; Andersen, R. A.; Copéret, C.; Eisenstein, O. Carbon-13 NMR chemical shift: A descriptor for electronic structure and reactivity of organometallic compounds. *Acc. Chem. Res.* **2019**, *52*, 2278−2289.
(18) Venkatesh, A.; Lund, A.; Rochlitz, L.; Jabbour, R.; Gordon, C. P.; Menzildjian, G.; Viger-Gravel, J.; Berruyer, P.; Gajan, D.; Copéret, C.; et al. The structure of molecular and surface platinum sites determined by DNP-SENS and fast MAS ^{195}Pt Solid-State NMR spectroscopy. *J. Am. Chem. Soc.* **2020**, *142*, 18936−18945.
(19) Venkatesh, A.; Gioffrè, D.; Atterberry, B. A.; Rochlitz, L.; Carnahan, S. L.; Wang, Z.; Menzildjian, G.; Lesage, A.; Copéret, C.; Rossini, A. J. Molecular and electronic structure of isolated platinum sites enabled by the expedient measurement of ^{195}Pt chemical shift anisotropy. *J. Am. Chem. Soc.* **2022**, *144*, 13511−13525.
(20) Soorholtz, M.; Jones, L. C.; Samuelis, D.; Weidenthaler, C.; White, R. J.; Titirici, M.-M.; Cullen, D. A.; Zimmermann, T.; Antonietti, M.; Maier, J.; et al. Local platinum environments in a solid analogue of the molecular Periana catalyst. *ACS Catal.* **2016**, *6*, 2332−2340.
(21) Tang, J. A.; Kogut, E.; Norton, D.; Lough, A. J.; McGarvey, B. R.; Fekl, U.; Schurko, R. W. Impact of reduction on the properties of metal bisdithiolenes: Multinuclear solid-state NMR and structural studies on Pt(tfd)$_2$ and its reduced Forms. *J. Phys. Chem. B* **2009**, *113*, 3298−3313.
(22) Harris, R. K.; Reams, P.; Packer, K. J. High-resolution solid-state platinum-195 nuclear magnetic resonance. *Dalton Trans.* **1986**, 1015−1020.
(23) Hudson, Z. M.; Sun, C.; Harris, K. J.; Lucier, B. E. G.; Schurko, R. W.; Wang, S. Probing the structural origins of vapochromism of a triarylboron-functionalized platinum(II) acetylide by optical and multinuclear solid-state NMR spectroscopy. *Inorg. Chem.* **2011**, *50*, 3447−3457.
(24) Kogut, E.; Tang, J. A.; Lough, A. J.; Widdifield, C. M.; Schurko, R. W.; Fekl, U. Neutral high-potential nickel triad bisdithiolenes: Structure and solid-state NMR properties of Pt[$S_2C_2(CF_3)_2$]$_2$. *Inorg. Chem.* **2006**, *45*, 8850−8852.
(25) Lucier, B. E. G.; Johnston, K. E.; Xu, W.; Hanson, J. C.; Senanayake, S. D.; Yao, S.; Bourassa, M. W.; Srebro, M.; Autschbach, J.; Schurko, R. W. Unravelling the structure of Magnus' Pink Salt. *J. Am. Chem. Soc.* **2014**, *136*, 1333−1351.
(26) Todisco, S.; Saielli, G.; Gallo, V.; Latronico, M.; Rizzuti, A.; Mastrorilli, P. ^{31}P and ^{195}Pt solid-state NMR and DFT studies on platinum(i) and platinum(ii) complexes. *Dalton Trans.* **2018**, *47*, 8884−8891.
(27) Mastrorilli, P.; Todisco, S.; Bagno, A.; Gallo, V.; Latronico, M.; Fortuño, C.; Gudat, D. Multinuclear solid-state NMR and DFT studies on phosphanido-bridged diplatinum complexes. *Inorg. Chem.* **2015**, *54*, 5855−5863.
(28) Roukala, J.; Orr, S. T.; Hanna, J. V.; Vaara, J.; Ivanov, A. V.; Antzutkin, O. N.; Lantto, P. Experimental and first-principles NMR analysis of Pt(II) complexes with *O,O′*-dialkyldithiophosphate ligands. *J. Phys. Chem. A* **2016**, *120*, 8326−8338.
(29) Lucier, B. E. G.; Reidel, A. R.; Schurko, R. W. Multinuclear solid-state NMR of square-planar platinum complexes — Cisplatin and related systems. *Can. J. Chem.* **2011**, *89*, 919−937.
(30) Sparks, S. W.; Ellis, P. D. ^{195}Pt shielding tensors in potassium hexachloroplatinate(IV) and potassium tetrachloroplatinate(II). *J. Am. Chem. Soc.* **1986**, *108*, 3215−3218.
(31) Peters, G.; Preetz, W.; Schaller, T.; Sebald, A. ^{19}F−^{195}Pt double-resonance MAS NMR experiments on polycrystalline salts $M_2[PtF_6]$; (M = K, Cs, Rb, NMe_4). *J. Magn. Reson.* **1996**, *120*, 121−124.
(32) Ivanov, A. V.; Palazhchenko, V. I.; Strikha, V. E.; Antzutkin, O. N.; Forsling, W. Structural features and NMR ^{195}Pt spectroscopy of cooperite monocrystals (natural Pts). *Dokl. Earth Sci.* **2006**, *410*, 1141−1144.
(33) Rozhdestvina, V. I.; Ivanov, A. V.; Zaremba, M. A.; Antsutkin, O. N.; Forsling, W. Single-crystalline cooperite (PtS): Crystal-chemical characterization, ESR spectroscopy, and ^{195}Pt NMR spectroscopy. *Crystallogr. Rep.* **2008**, *53*, 391−397.
(34) Thibault, M.-H.; Lucier, B. E. G.; Schurko, R. W.; Fontaine, F.-G. Synthesis and solid-state characterization of platinum complexes with hexadentate amino- and iminophosphine ligands. *Dalton Trans.* **2009**, 7701−7716.
(35) Schurko, R. W. Ultra-wideline solid-state NMR spectroscopy. *Acc. Chem. Res.* **2013**, *46*, 1985−1995.
(36) MacGregor, A. W.; O'Dell, L. A.; Schurko, R. W. New methods for the acquisition of ultra-wideline solid-state NMR spectra of spin-1/2 nuclides. *J. Magn. Reson.* **2011**, *208*, 103−113.
(37) Altenhof, A. R.; Jaroszewicz, M. J.; Lindquist, A. W.; Foster, L. D. D.; Veinberg, S. L.; Schurko, R. W. Practical aspects of recording ultra-wideline NMR patterns under magic-angle spinning conditions. *J. Phys. Chem. C* **2020**, *124*, 14730−14744.
(38) Altenhof, A. R.; Lindquist, A. W.; Foster, L. D. D.; Holmes, S. T.; Schurko, R. W. On the use of frequency-swept pulses and pulses designed with optimal control theory for the acquisition of ultra-wideline NMR spectra. *J. Magn. Reson.* **2019**, *309*, 106612.
(39) Koppe, J.; Bußkamp, M.; Hansen, M. R. Frequency-swept ultra-wideline magic-angle spinning NMR spectroscopy. *J. Phys. Chem. A* **2021**, *125*, 5643−5649.
(40) Koppe, J.; Frerichs, J. E.; Hansen, M. R. Pushing the detection limit of static wideline NMR spectroscopy using ultrafast frequency-swept pulses. *J. Phys. Chem. Lett.* **2023**, *14*, 10748−10753.
(41) Harris, K. J.; Lupulescu, A.; Lucier, B. E. G.; Frydman, L.; Schurko, R. W. Broadband adiabatic inversion pulses for cross polarization in wideline solid-state NMR spectroscopy. *J. Magn. Reson.* **2012**, *224*, 38−47.
(42) Altenhof, A. R.; Jaroszewicz, M. J.; Harris, K. J.; Schurko, R. W. Broadband adiabatic inversion experiments for the measurement of longitudinal relaxation time constants. *J. Chem. Phys.* **2021**, *154*, 034202.
(43) Kobayashi, T.; Perras, F. A.; Goh, T. W.; Metz, T. L.; Huang, W.; Pruski, M. DNP-enhanced ultrawideline solid-state NMR spectroscopy: Studies of platinum in metal−organic frameworks. *J. Phys. Chem. Lett.* **2016**, *7*, 2322−2327.
(44) Rossini, A. J.; Hanrahan, M. P.; Thuo, M. Rapid acquisition of wideline MAS solid-state NMR spectra with fast MAS, proton detection, and dipolar HMQC pulse sequences. *Phys. Chem. Chem. Phys.* **2016**, *18*, 25284−25295.
(45) Jaroszewicz, M. J.; Altenhof, A. R.; Schurko, R. W.; Frydman, L. Sensitivity enhancement by progressive saturation of the proton reservoir: A solid-state NMR analogue of chemical exchange saturation transfer. *J. Am. Chem. Soc.* **2021**, *143*, 19778−19784.
(46) Bayzou, R.; Trébosc, J.; Hung, I.; Gan, Z.; Lafon, O.; Amoureux, J.-P. Indirect NMR detection via proton of nuclei subject to large anisotropic interactions, such as ^{14}N, ^{195}Pt, and ^{35}Cl, using the T-HMQC sequence. *J. Chem. Phys.* **2022**, *156*, 064202.
(47) Atterberry, B. A.; Wimmer, E.; Estes, D. P.; Rossini, A. J. Acceleration of indirect detection ^{195}Pt solid-state NMR experiments by sideband selective excitation or alternative indirect sampling schemes. *J. Magn. Reson.* **2023**, *352*, 107457.
(48) Venkatesh, A.; Perras, F. A.; Rossini, A. J. Proton-detected solid-state NMR spectroscopy of spin-1/2 nuclei with large chemical shift anisotropy. *J. Magn. Reson.* **2021**, *327*, 106983.
(49) Phillips, B. L.; Houston, J. R.; Feng, J.; Casey, W. H. Observation of solid-state ^{103}Rh NMR by cross-polarization. *J. Am. Chem. Soc.* **2006**, *128*, 3912−3913.
(50) Venkatesh, A.; Ryan, M. J.; Biswas, A.; Boteju, K. C.; Sadow, A. D.; Rossini, A. J. Enhancing the sensitivity of solid-state NMR experiments with very low gyromagnetic ratio nuclei with fast magic angle spinning and proton detection. *J. Phys. Chem. A* **2018**, *122*, 5635−5643.
(51) Ooms, K. J.; Wasylishen, R. E. Solid-state Ru-99 NMR spectroscopy: A useful tool for characterizing prototypal diamagnetic ruthenium compounds. *J. Am. Chem. Soc.* **2004**, *126*, 10972−10980.

https://doi.org/10.1021/acs.inorgchem.5c05169
Inorg. Chem. 2026, 65, 4430−4445

(52) Hooper, T. J. N.; Partridge, T. A.; Rees, G. J.; Keeble, D. S.; Powell, N. A.; Smith, M. E.; Mikheenko, I. P.; Macaskie, L. E.; Bishop, P. T.; Hanna, J. V. Direct solid state NMR observation of the 105Pd nucleus in inorganic compounds and palladium metal systems. *Phys. Chem. Chem. Phys.* **2018**, *20*, 26734−26743.
(53) Holmes, S. T.; Schönzart, J.; Philips, A. B.; Kimball, J. J.; Termos, S.; Altenhof, A. R.; Xu, Y.; O'Keefe, C. A.; Autschbach, J.; Schurko, R. W. Structure and bonding in rhodium coordination compounds: A ^{103}Rh solid-state NMR and relativistic DFT study. *Chem. Sci.* **2024**, *15*, 2181−2196.
(54) Holmes, S. T.; Xu, Y.; Philips, A. B.; Termos, S.; Kimball, J. J.; Autschbach, J.; Schurko, R. W. ^{99} Ru Solid-State Nuclear Magnetic Resonance Spectroscopy of Organometallic Compounds: Linking Nuclear Magnetic Resonance Parameters with Metal−Ligand Bonding. *J. Am. Chem. Soc.* **2025**, *147* (24), 20865−20877.
(55) Kimball, J. J.; Schurko, R. W. Acquisition of ^{1}H-detected ^{103}Rh and ^{99}Ru solid-state nuclear magnetic resonance spectra in stationary samples. *J. Phys. Chem. Lett.* **2025**, *16*, 4596−4601.
(56) Alkan, F.; Dybowski, C. Spin-orbit effects on the ^{125}Te magnetic-shielding tensor: A cluster-based ZORA/DFT investigation. *Solid State Nucl. Magn. Reson.* **2018**, *95*, 6−11.
(57) Holmes, S. T.; Schurko, R. W. A DFT/ZORA study of cadmium magnetic shielding tensors: Analysis of relativistic effects and electronic-state approximations. *J. Chem. Theory Comput.* **2019**, *15*, 1785−1797.
(58) Alkan, F.; Dybowski, C. Calculation of chemical-shift tensors of heavy nuclei: A DFT/ZORA investigation of ^{199}Hg chemical-shift tensors in solids, and the effects of cluster size and electronic-state approximations. *Phys. Chem. Chem. Phys.* **2014**, *16*, 14298−14308.
(59) Alkan, F.; Dybowski, C. Chemical-shift tensors of heavy nuclei in network solids: A DFT/ZORA investigation of ^{207}Pb chemical-shift tensors using the bond-valence method. *Phys. Chem. Chem. Phys.* **2015**, *17*, 25014−25026.
(60) Alkan, F.; Dybowski, C. Effect of co-ordination chemistry and oxidation state on the ^{207}Pb magnetic-shielding tensor: A DFT/ZORA investigation. *J. Phys. Chem. A* **2016**, *120*, 161−168.
(61) Alkan, F.; Holmes, S. T.; Dybowski, C. Role of exact exchange and relativistic approximations in calculating ^{19}F magnetic shielding in solids using a cluster *ansatz*. *J. Chem. Theory Comput.* **2017**, *13*, 4741−4752.
(62) Davis, J. C.; Bühl, M.; Koch, K. R. On the origin of $^{35/37}$Cl isotope effects on ^{195}Pt NMR chemical shifts. a density functional study. *J. Chem. Theory Comput.* **2012**, *8*, 1344−1350.
(63) Davis, J. C.; Bühl, M.; Koch, K. R. Probing isotope shifts in ^{103}Rh and ^{195}Pt NMR spectra with density functional theory. *J. Phys. Chem. A* **2013**, *117*, 8054−8064.
(64) Still, B. M.; Kumar, P. G. A.; Aldrich-Wright, J. R.; Price, W. S. ^{195}Pt NMR—theory and application. *Chem. Soc. Rev.* **2007**, *36*, 665−686.
(65) Gabano, E.; Marengo, E.; Bobba, M.; Robotti, E.; Cassino, C.; Botta, M.; Osella, D. ^{195}Pt NMR spectroscopy: A chemometric approach. *Coord. Chem. Rev.* **2006**, *250*, 2158−2174.
(66) Priqueler, J. R. L.; Butler, I. S.; Rochon, F. D. An overview of ^{195}Pt nuclear magnetic resonance spectroscopy. *Appl. Spectrosc. Rev.* **2006**, *41*, 185−226.
(67) Gilbert, T. M.; Ziegler, T. Prediction of ^{195}Pt NMR chemical shifts by density functional theory computations: The importance of magnetic coupling and relativistic effects in explaining trends. *J. Phys. Chem. A* **1999**, *103*, 7535−7543.
(68) Penka Fowe, E.; Belser, P.; Daul, C.; Chermette, H. Assessment of theoretical prediction of the NMR shielding tensor of $^{195}PtCl_xBr_{6-x}^{2-}$ complexes by DFT calculations: Experimental and computational results. *Phys. Chem. Chem. Phys.* **2005**, *7*, 1732−1738.
(69) Krykunov, M.; Ziegler, T.; van Lenthe, E. Implementation of a hybrid DFT method for calculating NMR shieldings using Slater-type orbitals with spin−orbital coupling included. applications to ^{187}Os, ^{195}Pt, and ^{13}C in heavy-metal complexes. *J. Phys. Chem. A* **2009**, *113*, 11495−11500.
(70) Atterberry, B. A.; Wimmer, E. J.; Klostermann, S.; Frey, W.; Kästner, J.; Estes, D. P.; Rossini, A. J. Structural characterization of surface immobilized platinum hydrides by sensitivity-enhanced ^{195}Pt solid state NMR spectroscopy and DFT calculations. *Chem. Sci.* **2025**, *16*, 1271−1287.
(71) Burger, M. R.; Kramer, J.; Chermette, H.; Koch, K. R. A comparison of experimental and DFT calculations of ^{195}Pt NMR shielding trends for $[PtX^nY_{6-n}]^{2-}$ (X, Y= Cl, Br, F and I) anions. *Magn. Reson. Chem.* **2010**, *48*, S38−S47.
(72) Autschbach, J.; Le Guennic, B. Solvent effects on ^{195}Pt and ^{205}Tl NMR chemical shifts of the complexes $[(NC)_5Pt-Tl(CN)_n]^{n-}$ (n = 0−3), and $[(NC)_5Pt-Tl-Pt(CN)_5]^{3-}$ studied by relativistic density functional theory. *Chem. − Eur. J.* **2004**, *10*, 2581−2589.
(73) Sterzel, M.; Autschbach, J. Toward an accurate determination of ^{195}Pt chemical shifts by density functional computations: The importance of unspecific solvent effects and the dependence of Pt magnetic shielding constants on structural parameters. *Inorg. Chem.* **2006**, *45*, 3316−3324.
(74) Truflandier, L. A.; Autschbach, J. Probing the solvent shell with ^{195}Pt chemical shifts: Density functional theory molecular dynamics study of Pt^{II} and Pt^{IV} anionic complexes in aqueous solution. *J. Am. Chem. Soc.* **2010**, *132*, 3472−3483.
(75) Truflandier, L. A.; Sutter, K.; Autschbach, J. Solvent effects and dynamic averaging of ^{195}Pt NMR shielding in cisplatin derivatives. *Inorg. Chem.* **2011**, *50*, 1723−1732.
(76) Van Lenthe, E.; Baerends, E. J.; Snijders, J. G. Relativistic regular two-component Hamiltonians. *J. Chem. Phys.* **1993**, *99*, 4597−4610.
(77) Le Guennic, B.; Autschbach, J. $[Pt@Pb_{12}]^{2-}$ — A challenging system for relativistic density functional theory calculations of ^{195}Pt and ^{207}Pb NMR parameters. *Can. J. Chem.* **2011**, *89*, 814−821.
(78) Batista, P. R.; Ducati, L. C.; Autschbach, J. Solvent effect on the ^{195}Pt NMR properties in pyridonate-bridged Pt^{III} dinuclear complex derivatives investigated by ab initio molecular dynamics and localized orbital analysis. *Phys. Chem. Chem. Phys.* **2021**, *23*, 12864−12880.
(79) Batista, P. R.; Ducati, L. C.; Autschbach, J. Dynamic and relativistic effects on Pt−Pt indirect spin−spin coupling in aqueous solution studied by ab initio molecular dynamics and two- vs four-component density functional NMR calculations. *J. Chem. Phys.* **2024**, *160* (11), 114307.
(80) Castro, A. C.; Balcells, D.; Repisky, M.; Helgaker, T.; Cascella, M. First-principles calculation of ^{1}H NMR chemical shifts of complex metal polyhydrides: The essential inclusion of relativity and dynamics. *Inorg. Chem.* **2020**, *59*, 17509−17518.
(81) Autschbach, J. The accuracy of hyperfine integrals in relativistic NMR computations based on the zeroth-order regular approximation. *Theor. Chem. Acc.* **2004**, *112*, 52−57.
(82) Autschbach, J. The role of the exchange-correlation response kernel and scaling corrections in relativistic density functional nuclear magnetic shielding calculations with the zeroth-order regular approximation. *Mol. Phys.* **2013**, *111*, 2544−2554.
(83) Arcisauskaite, V.; Melo, J. I.; Hemmingsen, L.; Sauer, S. P. A. Nuclear magnetic resonance shielding constants and chemical shifts in linear ^{199}Hg compounds: A comparison of three relativistic computational methods. *J. Chem. Phys.* **2011**, *135* (4), 044306.
(84) Wodyński, A.; Repiský, M.; Pecul, M. A comparison of two-component and four-component approaches for calculations of spin-spin coupling constants and NMR shielding constants of transition metal cyanides. *J. Chem. Phys.* **2012**, *137* (1), 014311.
(85) Vícha, J.; Novotný, J.; Straka, M.; Repisky, M.; Ruud, K.; Komorovsky, S.; Marek, R. Structure, solvent, and relativistic effects on the NMR chemical shifts in square-planar transition-metal complexes: Assessment of DFT approaches. *Phys. Chem. Chem. Phys.* **2015**, *17*, 24944−24955.
(86) Komorovsky, S.; Jakubowska, K.; Świder, P.; Repisky, M.; Jaszuński, M. NMR spin−spin coupling constants derived from relativistic four-component DFT theory—analysis and visualization. *J. Phys. Chem. A* **2020**, *124*, 5157−5169.

https://doi.org/10.1021/acs.inorgchem.5c05169
Inorg. Chem. 2026, 65, 4430−4445

(87) Bühl, M. NMR of transition metal compounds. In *Calculation of NMR and EPR Parameters: Theory and Applications*; Kaupp, M.; Bühl, M.; Malkin, V. G., Eds.; Wiley Online Library, 2004, pp. 421−431.
(88) Zwanziger, J. W.; Farrant, A. R.; Werner-Zwanziger, U. Relativistic effects on the magnetic shielding in solids: First-principles computation in a plane wave code. *J. Magn. Reson.* **2025**, *374*, 107861.
(89) Speelman, T.; Huebsch, M.-T.; Havenith, R. W. A.; Marsman, M.; de Wijs, G. A. NMR chemical shielding for solid-state systems using spin−orbit coupled ZORA GIPAW. *J. Chem. Phys.* **2025**, *163* (10), 104115.
(90) Adamo, C.; Barone, V. Toward chemical accuracy in the computation of NMR shieldings: The PBE0 model. *Chem. Phys. Lett.* **1998**, *298*, 113−119.
(91) Autschbach, J.; Ziegler, T. Nuclear spin−spin coupling constants from regular approximate relativistic density functional calculations. I. Formalism and scalar relativistic results for heavy metal compounds. *J. Chem. Phys.* **2000**, *113*, 936−947.
(92) Autschbach, J. Analysis of NMR Spectroscopic Parameters. In *NMR Spectroscopic Parameters: Theories and Models, Computational Codes and Calculations*; Aucar, G. A., Ed.; Royal Society of Chemistry, 2025; Vol.: *38*, pp. 303-338.
(93) Clark, S. J.; Segall, M. D.; Pickard, C. J.; Hasnip, P. J.; Probert, M. J.; Refson, K.; Payne, M. C. First principles methods using CASTEP. *Z. Kristallogr.* **2005**, *220*, 567−570.
(94) Pfrommer, B. G.; Côté, M.; Louie, S. G.; Cohen, M. L. Relaxation of crystals with the quasi-Newton method. *J. Comput. Phys.* **1997**, *131*, 233−240.
(95) Perdew, J. P.; Burke, K.; Ernzerhof, M. Generalized gradient approximation made simple. *Phys. Rev. Lett.* **1996**, *77*, 3865−3868.
(96) Vanderbilt, D. Soft self-consistent pseudopotentials in a generalized eigenvalue formalism. *Phys. Rev. B* **1990**, *41*, 7892−7895.
(97) Yates, J. R.; Pickard, C. J.; Payne, M. C.; Mauri, F. Relativistic nuclear magnetic resonance chemical shifts of heavy nuclei with pseudopotentials and the zeroth-order regular approximation. *J. Chem. Phys.* **2003**, *118*, 5746−5753.
(98) Monkhorst, H. J.; Pack, J. D. Special points for Brillouin-zone integrations. *Phys. Rev. B* **1976**, *13*, 5188−5192.
(99) Tkatchenko, A.; DiStasio, R. A.; Car, R.; Scheffler, M. Accurate and efficient method for many-body van der Waals interactions. *Phys. Rev. Lett.* **2012**, *108*, 236402.
(100) *ADF 2021.1: Theoretical Chemistry*; SCM, Vrije Universiteit: Amsterdam, The Netherlands, 2021.
(101) Baerends, E. J.; Aguirre, N. F.; Austin, N. D.; Autschbach, J.; Bickelhaupt, F. M.; Bulo, R.; Cappelli, C.; van Duin, A. C. T.; Egidi, F.; Fonseca Guerra, C.; Forster, A.; Franchini, M.; Goumans, T. P. M.; Heine, T.; Hellstrom, M.; Jacob, C. R.; Jensen, L.; Krykunov, M.; van Lenthe, E.; Michalak, A.; Mitoraj, M. M.; Neugebauer, J.; Nicu, V. P.; Philipsen, P.; Ramanantoanina, H.; Ruger, R.; Schreckenbach, G.; Stener, M.; Swart, M.; Thijssen, J. M.; Trnka, T.; Visscher, L.; Yakovlev, A.; van Gisbergen, S. The Amsterdam Modeling Suite. *J. Chem. Phys.* **2025**, *162*, 162501.
(102) Pickard, C. J.; Mauri, F. All-electron magnetic response with pseudopotentials: NMR chemical shifts. *Phys. Rev. B* **2001**, *63*, 245101−245113.
(103) Bonhomme, C.; Gervais, C.; Babonneau, F.; Coelho, C.; Pourpoint, F.; Azaïs, T.; Ashbrook, S. E.; Griffin, J. M.; Yates, J. R.; Mauri, F.; et al. First-principles calculation of NMR parameters using the gauge including projector augmented wave method: A chemist's point of view. *Chem. Rev.* **2012**, *112*, 5733−5779.
(104) Ditchfield, R. Self-consistent perturbation theory of diamagnetism. *Mol. Phys.* **1974**, *27*, 789−807.
(105) Wolinski, K.; Hinton, J. F.; Pulay, P. Efficient implementation of the gauge-independent atomic orbital method for NMR chemical shift calculations. *J. Am. Chem. Soc.* **1990**, *112*, 8251−8260.
(106) Rodriguez-Fortea, A.; Alemany, P.; Ziegler, T. Density functional calculations of NMR chemical chifts with the inclusion of spin−orbit coupling in tungsten and lead compounds. *J. Phys. Chem. A* **1999**, *103*, 8288−8294.
(107) Krykunov, M.; Ziegler, T.; Lenthe, E. V. Hybrid density functional calculations of nuclear magnetic shieldings using Slater-type orbitals and the zeroth-order regular approximation. *Int. J. Quantum Chem.* **2009**, *109*, 1676−1683.
(108) Wolff, S. K.; Ziegler, T.; van Lenthe, E.; Baerends, E. J. Density functional calculations of nuclear magnetic shieldings using the zeroth-order regular approximation (ZORA) for relativistic effects: ZORA nuclear magnetic resonance. *J. Chem. Phys.* **1999**, *110*, 7689−7698.
(109) Autschbach, J.; Zurek, E. Relativistic density-functional computations of the chemical shift of ^{129}Xe in Xe@C_{60}. *J. Phys. Chem. A* **2003**, *107*, 4967−4972.
(110) Adamo, C.; Barone, V. Toward reliable density functional methods without adjustable parameters: The PBE0 model. *J. Chem. Phys.* **1999**, *110*, 6158−6170.
(111) van Lenthe, E.; Baerends, E. J.; Snijders, J. G. Relativistic total energy using regular approximations. *J. Chem. Phys.* **1994**, *101*, 9783−9792.
(112) van Lenthe, E.; Baerends, E. J.; Snijders, J. G. Construction of the Foldy−Wouthuysen transformation and solution of the Dirac equation using large components only. *J. Chem. Phys.* **1996**, *105*, 2373−2377.
(113) van Lenthe, E.; van Leeuwen, R.; Baerends, E. J.; Snijders, J. G. Relativistic regular two-component Hamiltonians. *Int. J. Quantum Chem.* **1996**, *57*, 281−293.
(114) Visscher, L.; van Lenthe, E. On the distinction between scalar and spin−orbit relativistic effects. *Chem. Phys. Lett.* **1999**, *306*, 357−365.
(115) Greif, A. H.; Hrobárik, P.; Hrobáriková, V.; Arbuznikov, A. V.; Autschbach, J.; Kaupp, M. A relativistic quantum-chemical analysis of the trans influence on ^{1}H NMR hydride shifts in square-planar platinum(II) complexes. *Inorg. Chem.* **2015**, *54*, 7199−7208.
(116) Holmes, S. T.; Iuliucci, R. J.; Mueller, K. T.; Dybowski, C. Density functional investigation of intermolecular effects on ^{13}C NMR chemical-shielding tensors modeled with molecular clusters. *J. Chem. Phys.* **2014**, *141* (16), 164121.
(117) Holmes, S. T.; Iuliucci, R. J.; Mueller, K. T.; Dybowski, C. Critical analysis of cluster models and exchange-correlation functionals for calculating magnetic shielding in molecular solids. *J. Chem. Theory Comput.* **2015**, *11*, 5229−5241.
(118) Holmes, S. T.; Engl, O. G.; Srnec, M. N.; Madura, J. D.; Quiñones, R.; Harper, J. K.; Schurko, R. W.; Iuliucci, R. J. Chemical shift tensors of cimetidine form A modeled with density functional theory calculations: Implications for NMR crystallography. *J. Phys. Chem. A* **2020**, *124*, 3109−3119.
(119) Becke, A. D. A multicenter numerical integration scheme for polyatomic molecules. *J. Chem. Phys.* **1988**, *88*, 2547−2553.
(120) Franchini, M.; Philipsen, P. H. T.; Visscher, L. The Becke fuzzy cells integration scheme in the Amsterdam Density Functional program suite. *J. Comput. Chem.* **2013**, *34*, 1819−1827.
(121) Alkan, F.; Holmes, S. T.; Iuliucci, R. J.; Mueller, K. T.; Dybowski, C. Spin-orbit effects on the ^{119}Sn magnetic-shielding tensor in solids: A ZORA/DFT investigation. *Phys. Chem. Chem. Phys.* **2016**, *18*, 18914−18922.
(122) Holmes, S. T.; Alkan, F.; Iuliucci, R. J.; Mueller, K. T.; Dybowski, C. Analysis of the bond-valence method for calculating ^{29}Si and ^{31}P magnetic shielding in covalent network solids. *J. Comput. Chem.* **2016**, *37*, 1704−1710.
(123) Glendening, E. D.; Landis, C. R.; Weinhold, F. NBO 6.0: Natural bond orbital analysis program. *J. Comput. Chem.* **2013**, *34*, 1429−1437.
(124) Alderman, D. W.; Sherwood, M. H.; Grant, D. M. Comparing, modeling, and assigning chemical-shift tensors in the cartesian, irreducible spherical, and icosahedral representations. *J. Magn. Reson.* **1993**, *101*, 188−197.
(125) Milburn, G. H. W.; Truter, M. R. The crystal structures of cis- and trans-dichlorodiammineplatinum(II). *J. Chem. Soc. A* **1966**, 1609−1616.
(126) Cohen, A. J.; Mori-Sánchez, P.; Yang, W. Challenges for density functional theory. *Chem. Rev.* **2012**, *112*, 289−320.

https://doi.org/10.1021/acs.inorgchem.5c05169
Inorg. Chem. 2026, 65, 4430−4445

(127) Grutzner, J. B. Chemical shift theory. Orbital symmetry and charge effects on chemical shifts. In *Recent advances in organic NMR spectroscopy*; Norell Press, 1987; pp. 17−42.
(128) Forgeron, M. A. M.; Wasylishen, R. E.; Penner, G. H. Investigation of magnetic shielding in xenon difluoride using solid-state NMR spectroscopy and relativistic density functional theory. *J. Phys. Chem. A* **2004**, *108*, 4751−4758.
(129) Zurek, E.; Pickard, C. J.; Autschbach, J. Density functional study of the ^{13}C NMR chemical shifts in single-walled carbon nanotubes with Stone−Wales defects. *J. Phys. Chem. C* **2008**, *112*, 11744−11750.
(130) Wang, Z.; Völker, L. A.; Robinson, T. C.; Kaeffer, N.; Menzildjian, G.; Jabbour, R.; Venkatesh, A.; Gajan, D.; Rossini, A. J.; Copéret, C.; et al. Speciation and structures in Pt surface Sstes stabilized by N-heterocyclic carbene ligands revealed by dynamic nuclear polarization enhanced indirectly detected ^{195}Pt NMR spectroscopic signatures and fingerprint analysis. *J. Am. Chem. Soc.* **2022**, *144*, 21530−21543.
(131) Zhang, B.; Goh, T. W.; Kobayashi, T.; Jing, D.; Wu, X.; Chen, M.; Huang, W. Structure evolution of single-site Pt in a metal−organic framework. *J. Chem. Phys.* **2021**, *154* (9), 094710.
(132) Koppe, J.; Yakimov, A. V.; Gioffrè, D.; Usteri, M.-E.; Vosegaard, T.; Pintacuda, G.; Lesage, A.; Pell, A. J.; Mitchell, S.; Pérez-Ramírez, J.; et al. Coordination environments of Pt single-atom catalysts from NMR signatures. *Nature* **2025**, *642*, 613−619.

https://doi.org/10.1021/acs.inorgchem.5c05169
Inorg. Chem. 2026, 65, 4430−4445